

REVIEWS OF TOPICAL PROBLEMS PACS numbers: 42.50.Dv, 42.65.Lm, 42.65.Yj

Photon correlations and features of nonclassical optical fields in a squeezed vacuum state

R V Zakharov, O V Tikhonova

DOI: https://doi.org/10.3367/UFNe.2022.04.039181

Contents

Abstract. We discuss the spatial and spectral properties of electromagnetic fields in a squeezed vacuum state and consider photon correlations in such fields. We concentrate on a bright squeezed vacuum with a large mean number of photons per mode and both spatial and frequency multimode structures. A theoretical approach based on the introduction of independent Schmidt modes and their photon operators is considered, which allows analytically correctly describing any characteristics of the squeezed field, including photon correlations, in good agreement with experiment. We present methods for controlling the mode content, degree of squeezing, and entanglement of photons of the generated squeezed light, including the scheme of a nonlinear interferometer; their advantages and applied prospects are analyzed. We discuss applied problems where squeezed nonclassical states are realized: the dispersion characteristics of media in the THz frequency range and high-precision detection of weak phase and angular perturbations based on correlations between photons.

R V Zakharov [1,2,a], **O V Tikhonova** [1,2,b]

[1] Lomonosov Moscow State University, Faculty of Physics, Leninskie gory 1, str. 2, 119991 Moscow, Russian Federation

[2] Skobeltsyn Institute of Nuclear Physics, Lomonosov Moscow State University Leninskie gory 1, str. 2, 119234 Moscow, Russian Federation

E-mail: [a] roma1997z@mail.ru, [b] ovtikhonova@mail.ru

Received 26 August 2021, revised 13 April 2022
Uspekhi Fizicheskikh Nauk **193** (4) 406 – 436 (2023)
Translated by S Alekseev

Keywords: quantum optics, multiphoton squeezed states of light, nonclassical electromagnetic fields, photon correlations, Schmidt modes, photon entanglement, high-precision quantum measurements

1. Introduction

Current progress in experimental quantum optics and laser physics has allowed laboratory generation of nonclassical light fields of various types. One of the most interesting and promising states of light is squeezed light fields, which can be obtained, for example, in the process of parametric light scattering in media with quadratic nonlinearity, when one pump photon produces two (signal and idler) photons with the total energy equal to the energy of the initial pumping photon [1]. In the case of a low pump intensity and vacuum states of the signal and idler fields at the entrance of the crystal, spontaneous parametric scattering produces correlated photon pairs, usually called biphotons [2, 3]. Nonclassical light generated in such a process can actually be considered the result of parametric amplification of vacuum fluctuations of the signal and idler fields [1].

The phenomenon of spontaneous parametric scattering was first predicted and theoretically substantiated by Klyshko in 1966 [4] and was soon discovered by several experimental groups [5–7]. An important point is that photons in a biphoton pair are correlated in a number of parameters: space, frequency, and time. Correlations of the signal and idler fields in terms of the number of photons were theoretically predicted by Klyshko and Zel'dovich [8] and were then first observed experimentally in [9].

It is the presence of correlations between signal and idler photons that opens up the possibility of a wide use of such light in various practical applications. Correlated biphoton pairs are used to create various entangled states of an electromagnetic field. Based on biphoton states, so-called qudits, analogs of quantum bits of a higher dimension (3, 4, or more) have been obtained [10–25]. This is achieved by using different degrees of freedom of photons, such as polarization, frequency, and angular momentum projection. These states have a high degree of photon entanglement, which is of fundamental importance for the development of quantum communications and quantum information technologies. There are many quantitative criteria for entanglement. For 'pure' bipartite states, entanglement occurs if the total wave function cannot be represented as a product of one-particle functions of individual subsystems. For a three-body system, the entanglement among all the components is already quite difficult to quantify. The degree of entanglement of biphoton ququarts and qutrits was calculated in [23, 24] in various ways based on quantitative measures of entanglement, such as the Schmidt parameter, concurrence, relative entropy, and von Neumann mutual information. For mixed bipartite systems, various entanglement characteristics are used, such as entanglement of formation and negativity [26, 27]. The simplest example of entangled biphoton states is provided by the Bell polarization states used for experimental demonstration of the properties of nonclassical light, which underlie the algorithms of quantum teleportation of unknown states of light [28–32]. Entangled two-photon states are used in quantum metrology, quantum tomography, quantum memory, optical quantum communication, and quantum cryptography [33–40].

At a high pump intensity, which ensures a high parametric conversion coefficient, parametric superluminescence occurs [1]. Generated under these conditions are no longer individual biphoton pairs but multiphoton squeezed states of light, with a mean number of photons per mode that can be very large. Such states of light are in fact a macroscopic quantum object. Of greatest interest is the squeezed vacuum — multiphoton squeezed light obtained in stimulated parametric scattering in the case where the modes of the signal and idler fields are initially in the vacuum state [41–44]. In [43], nonclassical light was experimentally obtained in the squeezed vacuum state with the mean number of photons of the order of 10^{13} per mode. The resulting number of photons corresponds to a very high brightness of the generated nonclassical light, and this state is hence called a bright squeezed vacuum. Typically, such fields are multimode. Generated in the nondegenerate regime are not single pairs of photons but so-called twin beams. In this case, correlations among a large number of photons occur, which is the most important nonclassical property of such light [44–47]. Moreover, the intensities of the signal and idler beams are totally correlated. Although the large number of photons contained in each beam is subject to strong fluctuations, the change in the number of photons in conjugate beams occurs synchronously, such that the dispersion of the difference between the numbers of photons in the idler and signal channels is theoretically identically equal to zero. In experiment, this dispersion is nonzero due to various losses that strongly affect the squeezed states and can destroy their unique nonclassical properties, but even then the spread of values is much smaller than the shot noise. In addition, such light is characterized by a significant decrease in the variance of the difference/sum of field quadratures of correlated field modes compared to that in the vacuum state. This means the suppression of quantum fluctuations for the process of measuring the sum or difference field. The squeezing for such quadratures is determined by phase relations between the pump field and the generated nonclassical light field. The described properties are called 'two-mode squeezing.'

In the case of parametric scattering in a frequency-degenerate collinear regime, light can be generated in a squeezed vacuum state in a single mode. Here, the field state is a superposition of a large number of even-numbered Fock states and has a very wide and smoothly decreasing distribution over the number of photons, with a variance that depends quadratically on the mean number of photons. In such a field, the probability of detecting a large number of photons is nonzero, which is important for the excitation of multiphoton processes during the interaction of light with matter. The variance of one of the field quadratures is suppressed in the single-mode squeezed vacuum (and the variance of the other quadrature is simultaneously increased). This property, called quadrature squeezing, implies a noise level that is significantly less than the 'standard quantum limit.' This opens up new possibilities for various metrological applications and the implementation of ultra-precise measurements with reduced noise.

It also turns out that the generation of multiphoton states, which are a macroscopic analogue of two-photon Bell states, is possible at high parametric gain [44]. For one of these, the 'singlet' one, unique polarization properties have been found, consisting in zero fluctuations of all Stokes parameters and invariance with respect to polarization transformations [48–50].

Thus, a multiphoton (bright) squeezed vacuum has a number of unique properties, which are widely used in solving problems of quantum metrology [51], quantum imaging [52–55], optomechanics [56], high-precision measurements [57–62], and transmission and processing of quantum information [63]. An important advantage of the multiphoton squeezed vacuum is its multimode structure, which opens up new possibilities for encoding quantum information.

The multimode squeezed vacuum is a new object that has been studied insufficiently. Because of the correlations of a large number of photons with each other and the high mean values of the number of photons per mode, the theoretical analysis of their space–time and correlation properties is extremely difficult, but is at the same in high demand. One of the most promising theoretical approaches is the Schmidt mode formalism. A detailed study of the Schmidt formalism and an analysis of the properties of biphoton states (in the regime of spontaneous parametric scattering at small values of the conversion coefficient) were performed in [17, 22, 64–70]. In [71–73], a similar approach was used to analyze the spectral properties of the squeezed vacuum, but analytic results were obtained only in the perturbation theory framework. For the regime of high parametric gain, only numerical calculations have been carried out. Another theoretical approach that has been used is based on a generalization of the wave equation and Maxwell's equations for field operators, but the results can then only be obtained numerically, because a system of integro-differential equations has to be solved [74–76].

This review is devoted to a discussion of the spatial and spectral properties of the bright squeezed vacuum. We describe a theoretical approach based on the introduction of new collective independent Schmidt modes and the corresponding photon creation/annihilation operators, which allows analytically obtaining the evolution of these operators in the case of a bright squeezed vacuum and hence theoretically describing any characteristics of such squeezed light, including photon correlations. We discuss the spatial and frequency modes of such light fields in detail and analyze the methods for controlling the mode content, squeezing, and entanglement of photons of the generated squeezed light. In particular, the scheme of a nonlinear Mach–Zehnder interferometer, made of two consecutive nonlinear crystals, is discussed, and its advantages and application options are considered. We focus especially on the features of the THz-range squeezed vacuum generated in a highly nondegenerate parametric scattering regime. In conclusion, we discuss applied problems implemented on the basis of nonclassical fields in a squeezed vacuum state: high-precision measurements of the dispersion characteristics of media in the THz range and high-precision detection of small perturbations based on correlations between photons.

2. Parametric generation of light in a squeezed vacuum state and its theoretical description in the Schmidt mode formalism

2.1 Parametric light scattering in a nonlinear crystal

We consider the simplest scheme of parametric light generation in a nonlinear crystal (Fig. 1). When a pump photon interacts with a nonlinear medium, two photons are produced, the signal and idler, whose frequencies and wave vectors satisfy the energy and momentum conservation laws [1]

$$\omega_{\mathrm{s}} + \omega_{\mathrm{i}} - \omega_{\mathrm{p}} = 0\,, \tag{1}$$

$$\mathbf{k}_{\mathrm{s}} + \mathbf{k}_{\mathrm{i}} - \mathbf{k}_{\mathrm{p}} = 0\,, \tag{2}$$

where $\omega_{\mathrm{s,\,i,\,p}}$ and $\mathbf{k}_{\mathrm{s,\,i,\,p}}$ are the frequencies and wave vectors of the signal, idler, and pumping photons. Due to the presence of dispersion in nonlinear media, relations (1) and (2), which are in fact the phase-matching conditions for the process of parametric scattering, can be satisfied most easily in anisotropic nonlinear crystals, for example, in β-barium borate (BBO) or potassium titanyl phosphate (KTP) crystals. The phase matching conditions restrict only the sum of frequencies and wave vectors of the generated photons, and therefore the generation of signal and idler photons occurs in a wide range of spectrum and emission-angle distributions. But the simultaneous satisfaction of phase matching conditions is possible only at certain frequencies and wave vector directions. In the case of a weak violation of the phase matching conditions, the process of parametric scattering can also occur, but with a lower probability. The probability distribution of parametric scattering depending on the frequency and direction of the photon wave vectors forms the so-called frequency-angle spectrum of parametric scattering. We note that the generated photons can have coincident or different

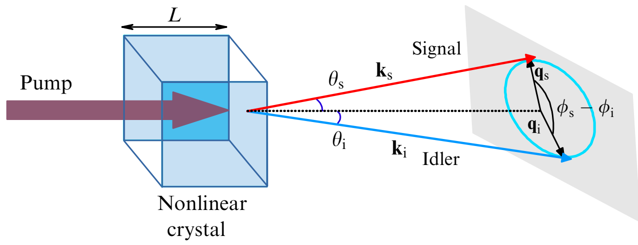

Figure 1. Parametric generation of light in a nonlinear crystal.

polarizations, which means phase matching of respective types I or II, with significantly different frequency–angle spectra [77]. If the signal and idler photons with exact phase matching have the same frequencies equal to half the pump frequency, $\omega_{\mathrm{s}} = \omega_{\mathrm{i}} = \omega_{\mathrm{p}}/2$, then the parametric scattering is called degenerate in frequency. In a strongly nondegenerate regime, the photon energies differ significantly from each other, such that one of the photons can even correspond to the THz frequency range. This regime shows a number of features to be discussed in Section 4.

The Hamiltonian of parametric light scattering in a crystal with a quadratic nonlinearity for both spontaneous and stimulated regimes can be represented as [1]

$$H \sim \int \mathrm{d}^3\mathbf{r}\,\chi^{(2)}(\mathbf{r})\,E_{\mathrm{p}}^{+}(\mathbf{r},t)\,E_{\mathrm{s}}^{-}(\mathbf{r},t)\,E_{\mathrm{i}}^{-}(\mathbf{r},t) + \mathrm{h.c.}\,, \tag{3}$$

where $\chi^{(2)}$ is the second-order nonlinear susceptibility, the subscripts s, i, and p denote the signal, idler, and pump fields, and the superscripts $(+\,-)$ correspond to positive- and negative-frequency parts of the field operators (respectively to photon absorption and emission). We note that squeezed states can also be obtained in the process of four-wave mixing that occurs in media with cubic nonlinearity. In this case, the Hamiltonian is similar to Hamiltonian (3), with $\chi^{(2)}$ replaced with a third-order nonlinear susceptibility and the second power of the pump field [78]. We analyze the process of parametric scattering in one nonlinear BBO crystal in the frequency-degenerate regime under the condition of smallness or compensation of anisotropy [79, 80]. Assuming monochromatic waves and zero frequency detuning, the Hamiltonian of the system can be written as

$$H = \mathrm{i}\hbar\Gamma \int \mathrm{d}\mathbf{q}_{\mathrm{s}}\mathrm{d}\mathbf{q}_{\mathrm{i}}\,F(\mathbf{q}_{\mathrm{s}},\mathbf{q}_{\mathrm{i}})a^{\dagger}_{\mathbf{q}_{\mathrm{s}}}a^{\dagger}_{\mathbf{q}_{\mathrm{i}}} + \mathrm{h.c.}\,, \tag{4}$$

where Γ is a parameter that characterizes the nonlinear interaction strength and depends on the nonlinearity of the crystal, and $F(\mathbf{q}_{\mathrm{s}},\mathbf{q}_{\mathrm{i}})$ is the biphoton amplitude, which in the case of identical frequencies and polarizations of the signal and idler photons depends on the transverse photon wave vectors $\mathbf{q}_{\mathrm{s}}$ and $\mathbf{q}_{\mathrm{i}}$ as [81–84]

$$F(\mathbf{q}_{\mathrm{s}},\mathbf{q}_{\mathrm{i}}) = C\,\exp\left[-\frac{\sigma^2(\mathbf{q}_{\mathrm{s}}+\mathbf{q}_{\mathrm{i}})^2}{2}\right]\mathrm{sinc}\left[\frac{L(\mathbf{q}_{\mathrm{s}}-\mathbf{q}_{\mathrm{i}})^2}{4k_{\mathrm{p}}}\right] \times \exp\left[-\,\mathrm{i}\left(\frac{L(\mathbf{q}_{\mathrm{s}}-\mathbf{q}_{\mathrm{i}})^2}{4k_{\mathrm{p}}}\right)\right]. \tag{5}$$

Here, L is the crystal length, $2\sqrt{\ln 2}\sigma$ is the full width at half maximum (FWHM) of the Gaussian spatial pump profile, and $\mathbf{k}_{\mathrm{p}}$ is the pump wave vector.

We note that biphoton amplitude (5) does not factor into the degrees of freedom of the signal and idler photons, which means that they are highly entangled. This significantly complicates the theoretical analysis of the properties of the generated squeezed fields.

One of the methods to analyze such fields theoretically is the perturbative approach. It is valid under conditions of weak pumping and allows obtaining the state vector of the spontaneous parametric scattering field in the first order with respect to the interaction operator [2, 85]:

$$|\Psi\rangle \propto |0\rangle + \int \mathrm{d}\mathbf{q}_\mathrm{s} \int \mathrm{d}\mathbf{q}_\mathrm{i}\, F(\mathbf{q}_\mathrm{s}, \mathbf{q}_\mathrm{i})\, a^\dagger_{\mathbf{q}_\mathrm{s}}\, a^\dagger_{\mathbf{q}_\mathrm{i}} |0\rangle\,. \tag{6}$$

Such a field characterizes the creation of biphotons or pairs of correlated photons with different distributions over transverse wave vectors. However, at a high pumping intensity, in the regime of parametric superluminescence [1], photons are generated not only in pairs: four, eight, or more photons correlated with each other can be produced. A multimode bright state of a squeezed vacuum formed in this process has a large number of photons that exhibit multiple spatial-frequency correlations with each other. Unlike biphoton pairs, such bright squeezed states cannot be described perturbatively, while the analysis of strong entanglement between photons in different modes is a separate difficult problem. Hence, there is a need to develop new nonperturbative theoretical methods and approaches to properly take the correlations among a large number of photons into account.

One such theoretical approach, developed in [81, 86], allows describing both spatial [81] and spectral [86] properties of the squeezed vacuum as well as photon correlations, and also allows obtaining analytic expressions for any measurable characteristic of such light. This approach is based on the introduction of new independent 'broadband' modes in terms of angle or frequency variables and the corresponding photon creation/annihilation operators in a given mode.

2.2 Spatial Schmidt modes and the evolution of their photon operators

As shown in Section 2.1, the photon field can be described in the formalism of plane waves having fixed frequency and direction of the photon wave vector. But in the case of the bright squeezed vacuum, such modes are strongly entangled, which fundamentally complicates the theoretical description of the properties of light. One of the possible ways to solve this problem is the introduction of new spatial–frequency modes, which are independent and actually diagonalize Hamiltonian (4). Such modes, called Schmidt modes, characterize the creation/annihilation of a photon in a continuous range of frequencies and emission angles. The formalism of Schmidt modes, originally introduced by Schmidt [87], is widely used in the study of bipartite systems of various natures [64, 88–91].

The most detailed analysis of Schmidt decomposition for bipartite systems was carried out in [67]. Schmidt decomposition can be defined as follows. For bipartite function $\Psi(x_1, x_2)$ a unique decomposition exists in the form

$$\Psi(x_1, x_2) = \sum_n \lambda_n^{1/2}\, \psi_n(x_1) f_n(x_2)\,. \tag{7}$$

The functions appearing in the decomposition are the Schmidt modes, and the decomposition coefficients determine the weights λ_n of these modes, which satisfy the normalization condition

$$\sum_n \lambda_n = 1\,. \tag{8}$$

A decomposition analogous to Schmidt decomposition (7) was also obtained by Mercer, but several years later [92]. It follows from Schmidt decomposition (7) that, for bipartite state $\Psi(x_1, x_2)$, the Schmidt-mode basis diagonalizes the reduced density matrices for each individual subsystem. In the most systematic way, the Schmidt modes, including phases, can be deduced from the integral equations [67]

$$\begin{aligned} &\int \mathrm{d}x_2\, \Psi(x_1, x_2) f_n^*(x_2) = \lambda_n^{1/2}\, \psi_n(x_1)\,, \\ &\int \mathrm{d}x_1\, \psi_n^*(x_1) \Psi(x_1, x_2) = \lambda_n^{1/2} f_n(x_2)\,. \end{aligned} \tag{9}$$

If the variables x_1 and x_2 take a discrete set of values, then the Schmidt decomposition is directly related to the singular value decomposition procedure known in linear matrix algebra [67]. The main advantage of using the Schmidt decomposition is the possibility of diagonalizing the problem and analyzing the entanglement and correlations that arise in a bipartite system.

To quantify entanglement in such a bipartite system, the Schmidt parameter is introduced as

$$K = \frac{1}{\sum_n \lambda_n^2}\,. \tag{10}$$

The minimum value of the Schmidt parameter is equal to unity, which means that the individual subsystems are then independent of each other and the total wave function can be factored into a product of one-particle states. The maximum entanglement in pure state (7) can be achieved if each subsystem is described by a reduced density matrix corresponding to a diagonal-type maximum-mixed state with diagonal elements of the same magnitude. The maximum value of the Schmidt parameter is therefore determined by the dimension of the basis of states of an individual subsystem.

Finding the Schmidt modes of the signal and idler photons from biphoton amplitude (5), which depends on four variables, is formally a difficult mathematical problem, because the Schmidt decomposition is unique only in the case of a two-variate function. However, the periodicity property of a function with respect to the difference between the azimuthal angles of photons allows obtaining its decomposition in azimuthal channels analytically:

$$F(q_\mathrm{s}, q_\mathrm{i}, \phi_\mathrm{s} - \phi_\mathrm{i}) = \sum_n \chi_n(q_\mathrm{s}, q_\mathrm{i}) \exp\left[\mathrm{i}n(\phi_\mathrm{s} - \phi_\mathrm{i})\right]. \tag{11}$$

Given this decomposition, it is already possible to use the Schmidt formalism [67, 84, 87–89] and represent each azimuthal channel function $\chi_n(q_\mathrm{s}, q_\mathrm{i})$ with the number n as a decomposition with respect to the 'radial' modes of the signal and idler photons, depending only on the absolute value of the transverse wave vector of each photon:

$$\chi_n(q_\mathrm{s}, q_\mathrm{i}) = \sum_{n,p} \sqrt{\lambda_{n,p}}\, \frac{u_{n,p}(q_\mathrm{s})}{\sqrt{q_\mathrm{s}}}\, \frac{v_{n,p}(q_\mathrm{i})}{\sqrt{q_\mathrm{i}}}\,. \tag{12}$$

The decomposition coefficients are determined by the mode weights $\lambda_{n,p}$, which satisfy the obvious normalization condition $\sum \lambda_{n,p} = 1$.

Thus, the following set of Schmidt modes, orthonormal in two-dimensional space, arises for the signal and idler photons [81–84]:

$$U_{n,p}(\mathbf{q}_s) = \frac{u_{n,p}(q_s)}{\sqrt{q_s}} \exp(\mathrm{i}n\phi_s)\,, \qquad V_{n,p}(\mathbf{q}_i) = \frac{u_{n,p}(q_i)}{\sqrt{q_i}} \exp(-\mathrm{i}n\phi_i)\,. \tag{13}$$

It is easy to see that the azimuthal modes $\exp(\mathrm{i}n\phi_s)$ correspond to photon states with a certain projection of the orbital angular momentum (OAM) on the z-axis, because they are eigenfunctions of the z-projection angular momentum operator with the eigenvalue $n\hbar$. Such light has a wavefront rotating about the z-axis in one direction or another, and is called 'twisted light.' Depending on the OAM, going around a circle in the xy plane gives rise to a phase shift equal to $2\pi n$. Moreover, in each azimuthal channel, the projections of the orbital momentum of the signal and idler photons are opposite. The 'radial' modes are the Laguerre–Gaussian functions in the simplest case of a single crystal [82, 83].

We note that spatial modes can be obtained not only in a polar but also in a Cartesian coordinate system. However, this is only possible if the sinc function in (5) is approximately replaced with a Gaussian profile [83]. The modes obtained in this way are approximate, although they factor into the product of Hermite–Gauss functions associated with the perpendicular directions of two-dimensional space.

Using modes (13), we can introduce new photon operators that describe the creation or annihilation of a signal or idler photon in a particular spatial Schmidt mode:

$$A^\dagger_{n,p} = \int \mathrm{d}\mathbf{q}_s U_{n,p}(\mathbf{q}_s)\, a^\dagger_{\mathbf{q}_s}\,, \quad B^\dagger_{n,p} = \int \mathrm{d}\mathbf{q}_i V_{n,p}(\mathbf{q}_i)\, a^\dagger_{\mathbf{q}_i}\,. \tag{14}$$

These operators satisfy the standard commutation relations

$$\left[A_{m,n}, A^\dagger_{k,l}\right] = \delta_{m,k}\,\delta_{n,l}\left[A_{m,n}, B^\dagger_{k,l}\right] = \delta_{m,k}\,\delta_{n,-l} \tag{15}$$

and describe the creation of photons with a certain projection of the orbital momentum on the z-axis, but only in a certain range of transverse wave vectors or polar angles corresponding to the 'radial' mode profile. The last commutation relation expresses the correlation of photons in conjugate beams with opposite OAM projections.

In terms of the introduced operators, the Hamiltonian of the parametric interaction can be expressed as

$$H = \mathrm{i}\hbar\Gamma \sum_{n,p} \sqrt{\lambda_{n,p}}\,(A^\dagger_{n,p}B^\dagger_{n,p} - A_{n,p}B_{n,p})\,, \tag{16}$$

and the operators themselves follow the Heisenberg-representation evolution [81, 93]

$$A^{\mathrm{out}}_{n,p} = A^{\mathrm{in}}_{n,p}\cosh\left(\sqrt{\lambda_{n,p}}\,G\right) + \left[B^{\mathrm{in}}_{n,p}\right]^\dagger \sinh\left(\sqrt{\lambda_{n,p}}\,G\right), \qquad B^{\mathrm{out}}_{n,p} = B^{\mathrm{in}}_{n,p}\cosh\left(\sqrt{\lambda_{n,p}}\,G\right) + \left[A^{\mathrm{in}}_{n,p}\right]^\dagger \sinh\left(\sqrt{\lambda_{n,p}}\,G\right), \tag{17}$$

where $G = \int \Gamma(t)\,\mathrm{d}t$ is the parametric gain coefficient, which is proportional to the pump amplitude. In the case of exact frequency matching, this approach involves no approximations, because the Hamiltonian is then independent of time.

The advantage of this approach is that the different Schmidt modes are independent, which allows diagonalizing the Hamiltonian and solving the problem even for an infinite number of modes. From a mathematical standpoint, this procedure allows passing from continuous spatial-angular variables to discrete characteristics, i.e., to the probability amplitudes and populations of various Schmidt modes.

The solutions obtained are in fact the Bogoliubov transformations for the Schmidt-mode photon operators. If the evolution of Schmidt operators (17) and the mode structure are known, we can obtain analytic expressions for any physical observables and the squeezed light characteristics of interest. For example, the intensity distribution in a signal beam has the form

$$\left\langle N_s(q_s)\right\rangle = \sum_{n,p} \frac{|u_{n,p}(q_s)|^2}{q_s} \sinh^2\left(G\sqrt{\lambda_{n,p}}\right). \tag{18}$$

The result obtained is an incoherent sum of distributions of individual Schmidt modes with new weights that depend on the parametric gain efficiency, and in fact on the pump field amplitude, the nonlinear susceptibility, and the crystal length. We note that $G\sqrt{\lambda_{0,0}}$ corresponds to the parametric gain coefficient commonly used in experiment [93].

The normalized effective weights of the Schmidt modes in (18) can be expressed as

$$\Lambda_{n,p} = \frac{\sinh^2\left(G\sqrt{\lambda_{n,p}}\right)}{\sum_{n,p}\sinh^2\left(G\sqrt{\lambda_{n,p}}\right)}\,. \tag{19}$$

We can introduce the effective weight of a single only-azimuthal or only-radial mode as

$$\Lambda_n = \sum_p \Lambda_{n,p}\,, \tag{20}$$

$$\Lambda_p = \sum_n \Lambda_{n,p}\,. \tag{21}$$

The values of the respective Schmidt parameters [67, 87–89] characterizing the entanglement of signal and idler photons in terms of azimuthal and radial variables can be calculated as [81, 93]

$$K_{\mathrm{az}} = \frac{1}{\sum_n \Lambda_n^2}\,, \qquad K_{\mathrm{rad}} = \frac{1}{\sum_p \Lambda_p^2}\,. \tag{22}$$

The degree of photon entanglement in all spatial variables is determined by the value of the total Schmidt parameter

$$K_{\mathrm{tot}} = \frac{1}{\sum_{n,p}\Lambda^2_{n,p}}\,. \tag{23}$$

As in (8), the sum of all weights of the Schmidt modes is equal to unity. Hence, the more effective weights make sizeable contributions to sums (22) and (23), the smaller the denominator in (22), (23) and the larger the Schmidt parameter. Therefore, the greater the number of spatial Schmidt modes, the higher the degree of spatial entanglement of photons. It hence follows that, with a fairly good accuracy, the Schmidt parameter can be interpreted not only as a quantitative measure of photon entanglement but also as an estimate of the effective number of spatial modes.

In this approach, therefore, the field in the signal and idler beams can be represented in terms of Schmidt modes with weights that are essentially dependent on the parametric gain coefficient. This allows varying the properties, including entanglement, of the photons of the detected squeezed vacuum, depending on the parametric conversion efficiency.

2.3 Frequency Schmidt modes

An approach similar to that described in Section 2.2 can also be developed in the spectral representation. In the case of one spatial mode, assuming a Gaussian temporal pumping profile, we can obtain an expression for a Hamiltonian similar to Hamiltonian (4) in the spatial case, but now in frequency variables [86]:

$$H = \mathrm{i}\hbar\Gamma \int \mathrm{d}\omega_{\mathrm{s}}\, \mathrm{d}\omega_{\mathrm{i}}\, F(\omega_{\mathrm{s}}, \omega_{\mathrm{i}}) a^{\dagger}_{\omega_{\mathrm{s}}} a^{\dagger}_{\omega_{\mathrm{i}}} + \mathrm{h.c.} \tag{24}$$

The biphoton spectral amplitude has the form

$$F(\omega_{\mathrm{s}}, \omega_{\mathrm{i}}) = C \exp\left[-\frac{(\omega_{\mathrm{s}} + \omega_{\mathrm{i}} - \omega_{\mathrm{p}})^2}{2\Omega^2}\right] \operatorname{sinc}\left(\frac{\Delta k L}{2}\right) \times \exp\left(-\mathrm{i}\,\frac{\Delta k L}{2}\right), \tag{25}$$

where $\Delta k = k_{\mathrm{p}}(\omega) - k_{\mathrm{s}}(\omega_{\mathrm{s}}) - k_{\mathrm{i}}(\omega_{\mathrm{i}})$ is the longitudinal mismatch of the wave vectors of the signal, idler, and pump photons, and Ω is the spectral width of the Gaussian profile of the pump amplitude.

The spectral amplitude of a biphoton, in contrast to that in the spatial case, can be immediately expanded in terms of one-dimensional frequency Schmidt modes [86]:

$$F(\omega_{\mathrm{s}}, \omega_{\mathrm{i}}) = \sum_n \sqrt{\lambda_n}\, u_n(\omega_{\mathrm{s}})\, v_n(\omega_{\mathrm{i}})\,. \tag{26}$$

Furthermore, by analogy with the spatial case, photon creation/annihilation operators in the Schmidt modes can be introduced. The Hamiltonian and the evolution of photon operators in the Heisenberg representation have a form similar to (16) and (17). The spectral Schmidt modes, unlike those in the spatial case, are one-dimensional (bear a single index), and in the case of a single nonlinear crystal their profiles are close to one-dimensional Hermite–Gauss functions [65].

Thus, within this approach, it is possible to analytically obtain any spectral characteristic of the squeezed vacuum in a wide range of parametric gain, up to high values (ignoring pump depletion), which can then be compared with those measured in experiment. Broadband Schmidt frequency modes were also introduced in [72, 73, 94], but finite numerical values of the relevant parameters characterizing squeezed light turned out to be difficult to obtain.

2.4 Photon number correlation of twin beams

From the analysis of Hamiltonian (16) and the evolution of photon operators in the Schmidt modes, we can immediately see the main property of the generated squeezed vacuum: photon number correlation in the signal and idler channels. Indeed, for each specific Schmidt mode number, the operator of the difference between the numbers of signal and idler photons is an integral of motion. Therefore, the variance of the difference between the numbers of photons is the same at the input and output of the a nonlinear crystal. For a squeezed vacuum, therefore, given vacuum states at the entrance to the crystal, the theoretical value of the variance of the difference in the numbers of photons is identically zero. Because the Schmidt modes are independent, the same holds for all modes. This result implies strong correlations in the number of photons in the signal and idler twin beams, often referred to as two-mode squeezing. To characterize correlations in this case, it is convenient to use the noise reduction factor (NRF) proportional to the variance of the difference between the numbers of photons in the signal and idler beams, $D_{N_{\mathrm{s}}-N_{\mathrm{i}}}$, normalized to the total mean number of photons in the beams:

$$\mathrm{NRF} = \frac{D_{N_{\mathrm{s}}-N_{\mathrm{i}}}}{\langle N_{\mathrm{s}} + N_{\mathrm{i}} \rangle}\,. \tag{27}$$

The NRF values recorded in experiments, although nonzero, were much less than unity [37, 41, 44, 51, 52, 95–98]. The NRF values obtained experimentally in [95] were much lower than the shot noise level. An analysis of the NRF dependence on the size of the angular aperture limiting the output beams was also performed there. It turned out that the degree of two-mode squeezing increases with an increase in the aperture diameter. Thus, the greater the number of spatial 'plane-wave' modes that can be distinguished, the better the correlations and the smaller the NRF. The selection of one 'broadband' spatial–frequency mode of a two-mode squeezed vacuum with a mean number of photons of about 20 was implemented in [98]. Direct measurement of correlations in the number of photons showed significant suppression of the difference fluctuations, to a level below the shot noise. From the standpoint of quantum information encoding, the selected state has a high 'dimension,' comprising about 6400 elements.

2.5 Quadrature squeezing and entanglement in quadrature variables

In Section 2.2, we discussed spatial correlations of photons in the signal and idler beams. The degree of photon entanglement in azimuthal or 'radial' variables is then determined by the value of the corresponding Schmidt parameter (22). In the case where generation occurs in one spatial mode for each of the conjugate beams, the biphoton amplitude factors with respect to spatial variables of the signal and idler photons, the Schmidt parameter is identically equal to unity, and there is no spatial entanglement. However, two-mode squeezing, i.e., the correlation between the numbers of photons in the signal and idler channels discussed in Section 2.4 is preserved, as quantified by NRF factor (27). Another important nonclassical property of a squeezed vacuum is quadrature squeezing. For a more detailed understanding of this effect, we first consider the single-mode squeezed vacuum corresponding to the degenerate case of coincident frequencies and wave vectors of signal and idler photons. The parametric generation of such light is described by the Hamiltonian [99]

$$H = \mathrm{i}\hbar\,\frac{\Gamma}{2}\left[\exp(\mathrm{i}\varphi)(a^{\dagger})^2 - \exp(-\mathrm{i}\varphi)a^2\right], \tag{28}$$

where φ is the phase of the pump field at the entrance to the crystal and $a^{\dagger}$ is the photon creation operator in a single mode, whose evolution in the Heisenberg representation corresponds to the solution

$$a^{\dagger}_{\mathrm{out}} = a^{\dagger}_{\mathrm{in}} \cosh G + \exp(-\mathrm{i}\varphi)\, a_{\mathrm{in}} \sinh G\,. \tag{29}$$

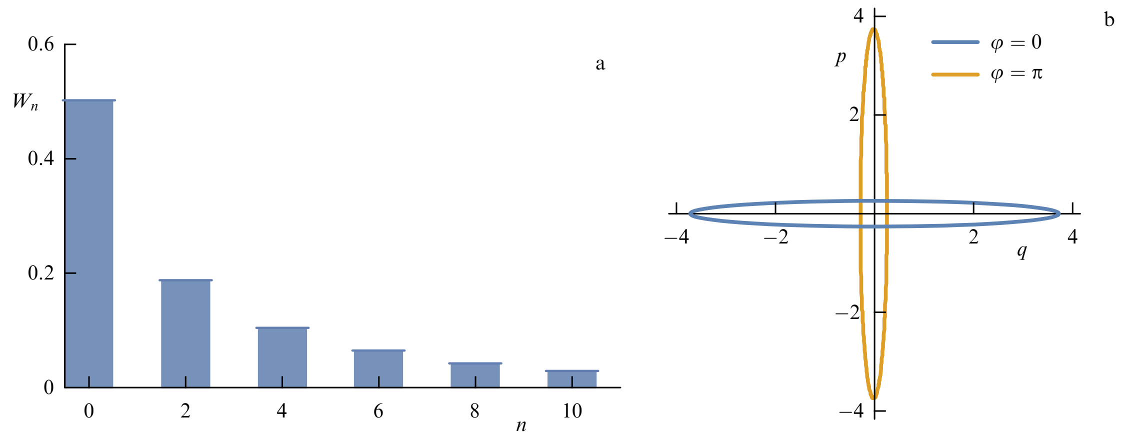

Figure 2. (a) Distribution over the number of photons and (b) Wigner function profile at half-height for two values of phase φ for state (30) with mean number of photons $\langle n \rangle = 3$.

Under these conditions, only an even number of photons can be produced, and the field state is a superposition of a large number of eigenstates of the field oscillator $|n\rangle$ with only even numbers and is characterized by a very wide smoothly decreasing distribution over the number of photons [99, 100]:

$$|\Psi_{\mathrm{s}}\rangle = \frac{1}{\sqrt{\cosh G}} \sum_{n=0}^{\infty} \exp(\mathrm{i}n\varphi) \tanh^n G \, \frac{\sqrt{(2n)!}}{2^n n!} \, |2n\rangle \, . \tag{30}$$

After the introduction of field quadratures

$$\widehat{X} = \frac{a + a^\dagger}{\sqrt{2}} \, , \qquad \widehat{P} = \frac{a - a^\dagger}{\mathrm{i}\sqrt{2}} \, , \tag{31}$$

state (30), depending on the coordinate quadrature at $\varphi = 0$, takes the form

$$\psi_{\mathrm{s}}(X) = \frac{1}{\pi^{1/4}\sqrt{R}} \exp\left[-\frac{1}{2}\left(\frac{X}{R}\right)^2\right], \tag{32}$$

with the parameter $R = \exp G$. It follows from (32) that, for large G, the variance of the coordinate field quadrature D_x, which can be represented as

$$D_x = \frac{R^2}{2} = \frac{1}{2} \exp(2G) \, , \tag{33}$$

is much greater than the variance of the vacuum state, which is equal to $1/2$.

Similarly, in the momentum representation, it follows that the variance of the momentum field quadrature is much less than in the vacuum state,

$$D_p = \frac{1}{2} \exp(-2G) \, . \tag{34}$$

Thus, a single-mode squeezed vacuum has suppressed variance along one of the field quadratures, which means that the level of fluctuations of this quadrature is much lower than the 'standard quantum limit,' and hence so-called quadrature squeezing occurs. Expressions for the variances of field quadratures can be obtained directly using the evolution of photon operators (29) in the Heisenberg representation. Depending on the phase difference φ, one or the other field quadrature is squeezed. In the general case, the quadrature 'rotated' through the angle $\beta = \pi/2 + \varphi/2$ is squeezed:

$$\widehat{X}_\beta = \widehat{X} \cos\beta + \widehat{P} \sin\beta = \frac{\exp(-\mathrm{i}\beta)\, a + \exp(\mathrm{i}\beta)\, a^\dagger}{\sqrt{2}} \, . \tag{35}$$

The distribution with respect to the number of photons and the Wigner function for state (30) are shown in Fig. 2 for the mean number of photons $\langle n \rangle = 3$. It can be seen that, at a phase equal to π, the coordinate quadrature is squeezed, which is accompanied by a strong increase in the variance of the momentum quadrature.

The regime of parametric generation of a two-mode squeezed vacuum, with each of the conjugate beams characterized by its unique mode, can be described by the Hamiltonian

$$H = \mathrm{i}\hbar\Gamma(a^\dagger b^\dagger - ab) \, , \tag{36}$$

where $a^\dagger$ and $b^\dagger$ are the photon creation operators in the signal and idler modes. The state vector of such a field can be written as a decomposition with respect to Fock states $|n\rangle_a$ and $|n\rangle_b$ with exact numbers of signal and idler photons [99, 100]:

$$|\Psi_t\rangle = \sum_{n=0}^{\infty} \frac{\tanh^n G}{\cosh G} \, |n\rangle_a |n\rangle_b \, . \tag{37}$$

In terms of the respective field quadratures X_a and X_b of the signal and idler fields, this state becomes

$$\Psi_R(X_a, X_b) = \frac{1}{\sqrt{\pi}} \exp\left[-\frac{(X_a - X_b)^2}{4R^2}\right] \times \exp\left[-\frac{R^2 (X_a + X_b)^2}{4}\right]. \tag{38}$$

By analogy with the conclusion deduced from the analysis of state (32), it follows from the form of function (38) that the sum of coordinate quadratures and the difference between the momentum quadratures of the signal and idler fields have suppressed variances. Moreover, their squeezing is characterized by the same factor:

$$R^{-2} = \exp(-2G) \, . \tag{39}$$

An important feature of the squeezed vacuum state (37) is that it cannot be represented as a product of individual wave functions of the signal and idler modes. This property, which means strong entanglement of twin beams, is often called entanglement in terms of the number of photons [44, 47, 101, 102]. This property should be distinguished from the above-described terminologically close concept of 'photon number correlation,' which refers to the synchronization of intensity fluctuations in both channels. We note that entanglement in the number of photons is directly related to entanglement in quadrature variables [102]. Indeed, wave function (38) cannot be factored with respect to the quadrature variables X_a and X_b of individual photons [102]. To quantify the photon entanglement in this state, it is convenient to use the fact that state (37) is also a Schmidt decomposition, but with the role of Schmidt modes played by the Fock states of the signal and idler modes, which depend on the quadrature variables of photons with the characteristic weights $æ_n = \tanh^{2n} G/\cosh^2 G$. In this case, it is therefore more convenient to use the Schmidt parameter as a measure of entanglement, although the negativity and other quantifiers also lead to correct results [44, 47, 101]. It follows from (37) that, the larger the mean number of photons, the more terms that appear in sum (37) and the higher the degree of entanglement. Indeed, with the weights found, the Schmidt parameter can be calculated by a formula similar to (10), and can be expressed in terms of the mean number of photons $\langle N \rangle$ in the signal or idler mode as [44, 102]

$$K = 2\langle N \rangle + 1 . \tag{40}$$

In the case of a multiphoton squeezed vacuum, with $\langle N \rangle \gg 1$, the degree of quadrature entanglement is actually determined by the aggregate number of photons in the signal and idler modes [102]. The direct relation between the noted entanglement in terms of the number of photons and the squeezing of the sum and difference quadratures of the field can be traced as follows. State (38) is entangled in the variables X_a and X_b and is factored with respect to the sum and difference quadratures with characteristic widths determined by their variances in this state. The degree of photon entanglement with respect to the field quadratures can be estimated based on the Fedorov parameter discussed in detail in Section 3.1, which is equal to the ratio of the widths of the single-particle unconditional and conditional distributions, which can easily be calculated from function (38) and lead to the result in (40). It can also be shown that Schmidt parameter (40) is equal to the arithmetic mean of the variances of the difference and sum quadratures in state (38). Thus, the entanglement of twin beams in terms of the number of photons or quadrature variables is directly related to the quadrature squeezing effect.

For a (space- or frequency-) multimode squeezed vacuum, entanglement in terms of the number of photons (quadrature variables) can also be calculated. In the case of independent Schmidt modes, the total entanglement is determined by the product of the Schmidt parameters (40) for each pair of conjugate modes. In the limit of a small mean number of photons per mode and a large number of modes, the product of Schmidt parameters (40) is proportional to the degree of entanglement in one mode and the effective number of modes [44]. For a bright multimode squeezed vacuum, in the limit of high parametric gain, the situation is more complicated, because the mean numbers of photons in different spatial modes differ greatly. Ignoring the contribution of spatial modes with the number of photons less than unity, we can obtain the following estimate for the logarithm of the Schmidt parameter, which in this case characterizes the entanglement in terms of the number of photons:

$$\ln K \sim 2G \sum \sqrt{\lambda_{n,p}} \, . \tag{41}$$

Here, the summation takes into account only spatial modes that are abundantly populated by photons. The resulting degree of entanglement significantly exceeds the degree of entanglement in the case of a single-mode bright squeezed vacuum and, unlike the latter, increases not linearly but as the square root of the effective number of modes due to the difference in their weights [101].

Let us discuss the possibility of measuring quadrature squeezing. In experiments, quadrature squeezing is often measured using the homodyne detection method, which is based on the fact that the investigated input field at the beam splitter is summed with the field of a local oscillator, which usually represents a coherent state with a large number of photons and a variable phase. As a result, the intensity in one of the output channels of the beam splitter, in addition to the noise of the local oscillator, contains an interference term proportional to the quadrature of the field under study. A more advanced method is balanced homodyne detection, in which the difference between the readings of photodetectors at the output of two channels of the beam splitter is measured. In that case, the noise of the local oscillator is entirely excluded, and fluctuations of the difference intensity are proportional to the fluctuations of the input field quadrature. Thus, when recording fluctuations of the output difference signal depending on the phase of the local oscillator, one can observe noise suppression to a level below the shot noise due to the squeezing effect for those phase values that correspond to the squeezed quadrature.

In [103], quadrature squeezing in various space-time modes of a generated multimode squeezed vacuum was measured by direct homodyne detection, and significant noise suppression, down to a level below shot noise, was obtained. Based on the results of experimental measurements for two selected spatial modes, the entries of the covariance matrix could be deduced.

In the experiment in [104], on the basis of quadrature squeezing in the spatial modes of the generated squeezed vacuum, noise suppression of the difference signal between two selected spatial pixels by about 2.5 dB was obtained. The detected spatial correlations were used to increase the accuracy of optical measurements of the position and spatial displacement of objects with an accuracy exceeding the standard quantum limit.

A similar idea was realized in the experiment in [105], where, for a spatial-multimode squeezed vacuum, quadrature squeezing was detected in 75 independent spatial regions with a size much smaller than the width of the transverse profile of the generated nonclassical light.

In [106], a wide-angle nonlinear Mach–Zehnder interferometer (often also called an SU(1,1) interferometer) was experimentally implemented, with a focusing lens placed between two nonlinear crystals. Because the bright squeezed vacuum coming out of the first nonlinear crystal and entering the second nonlinear crystal was focused by the lens, nonlinear amplification could be ensured in a wide range of the wave vector angles of squeezed light photons. Moreover, for all the mentioned directions, the magnitude of the phase shift that occurs in the interferometer between the pump and the signal and idler channel fields was the same, which allows simultaneously controlling many spatial modes in a wide angular range. The distribution of quadrature squeezing for various plane-wave modes at the output from the interferometer was obtained, and its value was recorded at the level of -4.3 dB.

The unique experiments that have been carried out testify to ample opportunities for using a squeezed vacuum to reduce the level of quantum noise in quantum measurements and quantum image recording problems.

3. Spatial properties of squeezed light

3.1 Properties of the squeezed vacuum generated in one nonlinear crystal

We consider spatial properties of a squeezed vacuum generated in one nonlinear crystal in the degenerate regime of parametric scattering with a biphoton amplitude in form (5).

In the case of weak pumping, in the formalism of the field state vector obtained in the perturbative framework, Eqn (6), the two-photon amplitude squared determines the joint probability distribution with respect to the signal and idler photon variables:

$$W_{pt}(\mathbf{q}_s, \mathbf{q}_i) = |F(q_s, q_i, \phi_s, \phi_i)|^2 . \tag{42}$$

The distribution with respect to the absolute values of the transverse wave vectors can be calculated by averaging over the azimuthal angles:

$$W(q_s, q_i) = \int d\phi_s \, d\phi_i \, |F(\mathbf{q}_s, \mathbf{q}_i)|^2 . \tag{43}$$

It is more convenient to change from transverse wave vectors to polar angles of photons in a crystal. The corresponding bipartite probability density as a function of the polar angles of the signal and idler photons is shown in Fig. 3a. The presented distribution demonstrates a strong correlation of photons: they have the same transverse wave vectors and, due to the frequency degeneracy, the same polar emission angles. The possible spread of the signal photon polar angles $\delta\theta_s$, measured experimentally or calculated from (43) at a fixed idler photon escape angle, is the radiation correlation width in the signal channel [85] (Fig. 3a). The correlation width of the idler channel radiation is determined similarly. Because the signal and idler photon frequencies coincide, the indicated correlation widths coincide in magnitude and are of the order of the width of the Gaussian function in (5). The total angular intensity distribution in each channel at the exit from the crystal can be calculated by averaging over all photon directions in the conjugate channel. The large angular width $\Delta\theta_{s,i}$ of this distribution, approximately corresponding to the width of the sinc function in (5), can be estimated as $1/\sqrt{k_s L}$ [85]. Thus, the signal width and the correlation width correspond to the widths of the unconditional and conditional distributions, respectively, obtained from bipartite distribution (43) by integrating over one of the variables and by fixing its value, as was discussed in detail in [44, 64, 65].

The parameter equal to the ratio of the signal width to the correlation width was first introduced by M V Fedorov to characterize entanglement in a bipartite system and bears his name. Fedorov also showed that this parameter is very close in magnitude to the Schmidt parameter [64, 65] and is therefore a good estimate of the characteristic number of Schmidt modes and photon entanglement. Indeed, the Schmidt parameter equal to unity corresponds to the distribution of both signal and idler photons in one spatial mode. Under these conditions, the correlation width is of the order of the total signal width. On the other hand, a small correlation width, i.e., a narrow conditional distribution at a fixed coordinate of the conjugate photon, can only be achieved for a large number of modes. The correlation width in Fig. 3a is much smaller than the total width of the spectrum, which, in accordance with the Fedorov parameter, allows predicting the presence of many modes. This result is confirmed by direct decomposition with respect to Schmidt modes, which is valid in both stimulated and spontaneous parametric scattering regimes, i.e., under conditions of weak pumping. Calculations in the limit of a small parametric gain $G \ll 1$ in Eqns (19)–(22) for the distribution shown in Fig. 3a give about 20 'radial' modes.

In the weak pumping regime, the distribution of photons over azimuthal angles can be calculated from the formula

$$W(\phi_s, \phi_i) = \int q_s \, dq_s q_i \, dq_i \, |F(\mathbf{q}_s, \mathbf{q}_i)|^2 . \tag{44}$$

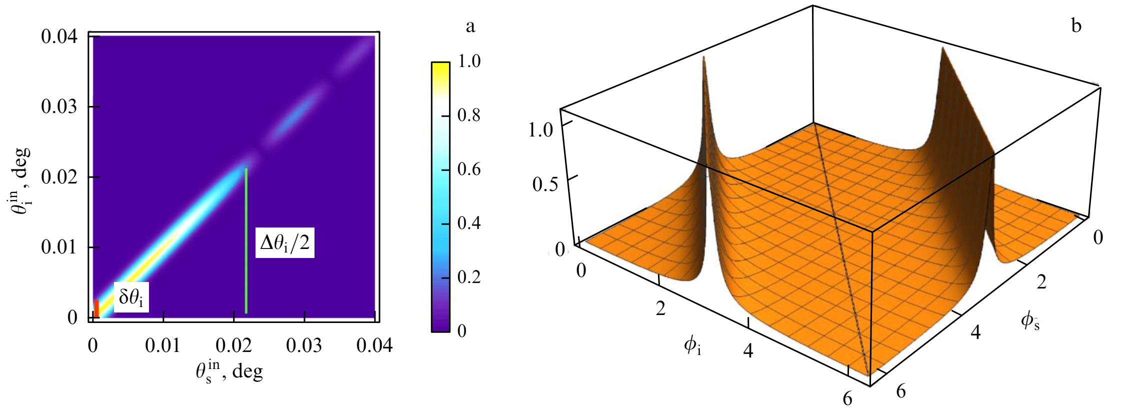

Figure 3. Bipartite probability density distribution for photons in (a) polar and (b) azimuthal angles of wave vectors in the limit of small parametric gain. FWHM spatial profile width is FWHM = 170 μm, crystal length $L = 2$ mm, $\lambda_s = \lambda_i = 800$ nm, $\lambda_p = 400$ nm.

The data presented in Fig. 3b demonstrate a strong correlation between the signal and idler photons in the azimuthal angles of their wave vectors shown in Fig. 1, in accordance with the condition $\phi_s - \phi_i = \pi$. The physical cause of this effect is easy to understand within the Schmidt mode formalism. The Schmidt mode phases involve the factor $(-1)^n = \exp(-in\pi)$ in each azimuthal channel in decomposition (12), and hence biphoton amplitude (11) is independent of the azimuthal angles of the signal and idler photons separately, but depends on the total argument $\phi_s - (\phi_i + \pi)$. This leads to the peaks at $\phi_s - \phi_i = \pi$ shown in the figure. Moreover, the peak width is inversely proportional to the characteristic number of azimuthal modes. Thus, it is most likely that the signal and idler photons have azimuthal angles differing by π, which means that photons with opposite transverse components of the wave vectors are correlated.

As mentioned above, the spatial distributions of photons obtained from the biphoton amplitude are only applicable in the perturbative regime. It is of interest to find how they change at a high pump intensity. This can be done using the formalism of Schmidt modes and the obtained solutions (17). According to a theoretical analysis, in the case of squeezed vacuum generation in a single crystal, as the parametric gain increases, the correlation width increases in both polar and azimuthal angles [101]. Hence, the photons remain correlated over an increasing range of angles. On the other hand, the effective number of spatial modes decreases, and therefore the contribution of the lowest, zeroth Schmidt mode increases, while the value of the Schmidt parameter characterizing the effective number of modes decreases. It thus follows that, as the pump intensity increases, the correlation width increases, which is accompanied by a decrease in the total signal width until one lowest Schmidt mode becomes dominant [81]. These effects are confirmed by experimental data [81]. However, in the experiment, to compensate for the anisotropy effects, two thinner closely spaced crystals were used instead of one nonlinear crystal. In a subsequent experiment with one nonlinear crystal, an increase in the total width of the angular spectrum by about 30% was detected [107]. The noted discrepancy with the theory occurs because the applicability of solutions (17) is limited by the exact frequency matching condition. In the experiment, there was entanglement, and the spatial and frequency degrees of freedom influenced each other. This effect was taken into account theoretically in [107] (see the discussion at the end of Section 6).

3.2 Control of the spatial properties in the scheme with a nonlinear interferometer

Controlling the spatial properties of a squeezed vacuum is important in various practical applications. This is realized by controlled changes in the weights and profiles of Schmidt modes. From this standpoint, the most promising and interesting system for study is the nonlinear Mach–Zehnder interferometer (Fig. 4), which is made of two sequentially arranged nonlinear crystals separated by some medium or just air [57, 81, 86, 106, 108–110]. In the literature, such an interferometer is often referred to as an SU(1,1) interferometer to emphasize the nonlinear nature of the parametric process, the possibility of using Lie algebra to describe it, and the connection between the photon operators at the entrance to and exit from the crystal via a Bogoliubov transformation. As shown below, the mode composition, shape, and number of Schmidt modes can be controlled in that system.

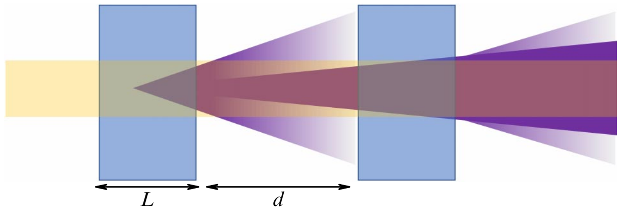

Figure 4. Nonlinear Mach–Zehnder interferometer made of two sequentially located nonlinear crystals of length L, separated by a distance d. Nonlinear transformation in the second crystal occurs only for radiation spatially overlapping with the pump.

A feature of the scheme involving an interferometer is that the nonlinear signal generated in the first crystal can be amplified or attenuated in the second crystal, depending on the acquired relative phases of the pump and signal/idler beams. An additional factor then occurs in the two-photon amplitude, a cosine that characterizes the phase interference effects, which depend on the distance d between crystals [81, 101, 111]:

$$F(\mathbf{q}_s, \mathbf{q}_i) = C \exp\left(-\frac{\sigma^2(\mathbf{q}_s + \mathbf{q}_i)^2}{2}\right) \operatorname{sinc}\left(\frac{L(\mathbf{q}_s - \mathbf{q}_i)^2}{4k_p}\right) \times \cos\left(\frac{L(\mathbf{q}_s - \mathbf{q}_i)^2}{4k_p} + \frac{\delta n k_s d}{n_s} + \frac{d(\mathbf{q}_s^{air} - \mathbf{q}_i^{air})^2}{4k_p^{air}}\right) \times \exp\left\{-i\left[\frac{L(\mathbf{q}_s - \mathbf{q}_i)^2}{2k_p} + \frac{\delta n k_s d}{n_s} + \frac{d(\mathbf{q}_s^{air} - \mathbf{q}_i^{air})^2}{4k_p^{air}}\right]\right\}, \quad (45)$$

where $\mathbf{k}_{s,i,p}$ are the signal, idler, and pump wave vectors, $\mathbf{q}_{s,i,p}(\mathbf{q}_{s,i,p}^{air})$ are their transverse components in the crystal (air gap), $n_{s,i,p}$ are the refractive indices of these waves in the crystal, and $\delta n = n_p^{air} - (n_s^{air} + n_i^{air})/2$ is the difference between the refractive index of the pump and half the sum of the refractive indices of the signal and idler photons in air. We note that, for small photon polar angles,

$$\frac{(\mathbf{q}_s^{air} - \mathbf{q}_i^{air})^2}{4k_p^{air}} \approx n_s \frac{(\mathbf{q}_s - \mathbf{q}_i)^2}{4k_p}.$$

Figure 5 shows the modulus squared of the two-photon amplitude as a function of the external polar angles of the photons and the intensity distribution in the far zone for two different separations between the crystals.

Interference results in the appearance of additional maxima and minima in the biphoton amplitude distribution compared to the distribution shown in Fig. 3a. Moreover, for different values of the photon polar angles, different phase conditions are realized, leading to radiation attenuation or amplification in the second crystal. As a result, parametric generation is suppressed at certain polar angles of the wave vectors of the signal and idler photons, and the spatial distribution of the squeezed vacuum intensity in the far zone is then characterized by a set of 'rings' with a maximum or minimum at the beam center. It is important that the period of spatial oscillations of the biphoton amplitude and the relative phase between the pump and the signal and idler radiation, acquired in the inter-crystal air gap, change with distance between the crystals. As a consequence, at a large separation of the crystals, the number of 'rings' in the intensity distribution in the far zone increases significantly, and the intensity at the

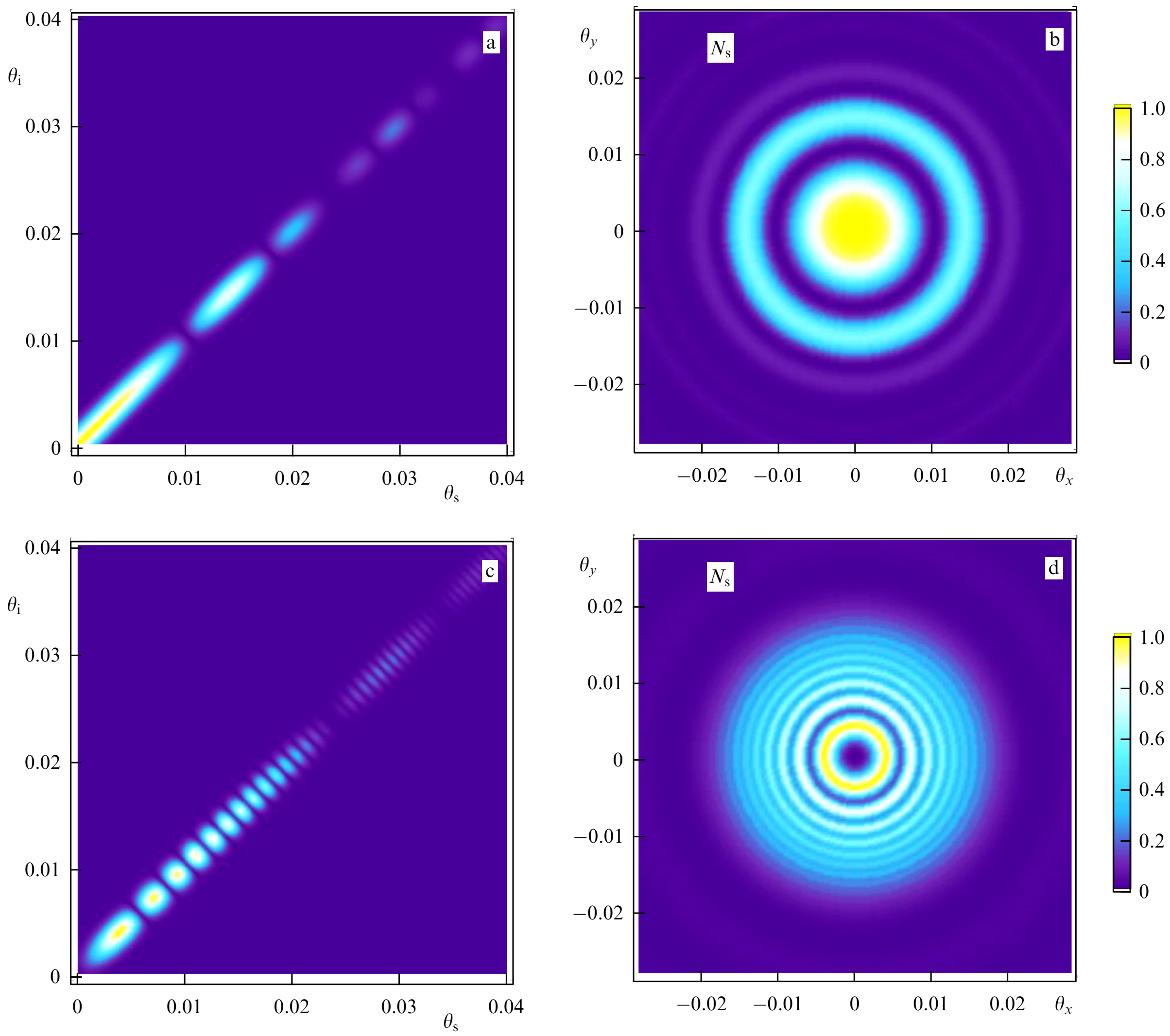

Figure 5. (a, c) Squared modulus of the two-photon amplitude depending on the external polar angles of photons and (b, d) intensity distribution in the far zone for the cases of (a, b) constructive and (c, d) destructive interference in the center of the beam, calculated for opposite azimuthal angles of photons. FWHM spatial profile width is FWHM = 170 μm, crystal length $L = 2$ mm, distance between crystals (a, b) $d = 2$ mm and (c, d) $d = 18$ mm, $\lambda_s = \lambda_i = 800$ nm, $\lambda_p = 400$ nm.

center of the beam is enhanced or suppressed, depending on constructive or destructive interference. Similar intensity distributions were also observed experimentally in [93, 108]. In the general case, in the scheme involving an interferometer, the Schmidt modes can differ significantly from the Laguerre–Gauss modes corresponding to the case of a single crystal, and searching for them is a separate problem.

For a small angular width of the spatial Gaussian pump profile compared with the longitudinal phase-matching width, a simplified expression for the biphoton amplitude depending on the polar and azimuthal angles was obtained in [101] in the form

$$F(\theta_s, \theta_i, \phi_s - \phi_i) = C \exp\left[-\frac{\theta_s^2 + \theta_i^2 + 2\theta_s\theta_i \cos(\phi_s - \phi_i)}{2a^2}\right] \times \operatorname{sinc}\left(\frac{\theta_s^2 + \theta_i^2}{b^2}\right) \cos\left(\frac{\theta_s^2 + \theta_i^2}{b_1^2} + \alpha\right) \times \exp\left\{-\mathrm{i}\left[\frac{\theta_s^2 + \theta_i^2}{b_2^2} + \alpha\right]\right\}, \tag{46}$$

where

$$a = \frac{c}{\sigma n_s \omega_s}, \quad b = \frac{2\sqrt{2}\, n_p}{n_s \sqrt{k_p L}}, \quad b_1 = \frac{2\sqrt{2}\, n_p}{n_s \sqrt{k_p (L + n_p d)}},$$

$$b_2 = \frac{2\sqrt{2} n_p}{n_s \sqrt{k_p (2L + n_p d)}},$$

and $\alpha = \delta n k_s d / n_s$ is the phase difference between the pump and the signal and idler radiation at the entrance to the second crystal, which, if necessary, can be additionally tuned in the experiment. The validity of the adopted approximations is ensured by the sharp maximum of the biphoton amplitude at $\phi_s - \phi_i = \pi$ and the small width of the Gaussian function in (46): $a \ll b$.

It follows from an analysis in (46) that the azimuthal modes of a squeezed vacuum are the same as in the case of a single crystal, and photons in conjugate beams are correlated for those azimuthal angles that differ by π. But the functions characterizing the azimuthal channels differ

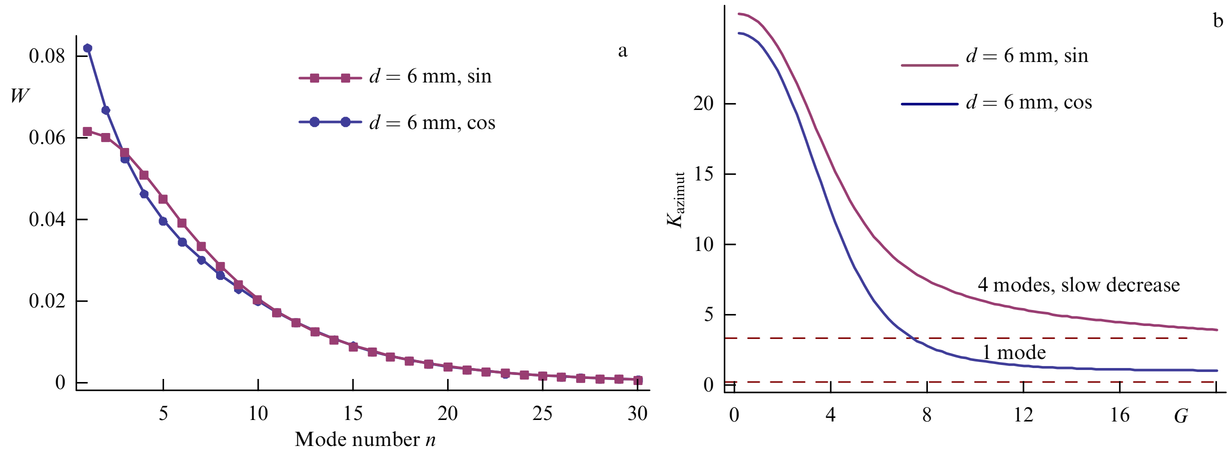

Figure 6. (a) Distribution over azimuthal modes and (b) effective number of azimuthal modes determined by the azimuthal Schmidt parameter, depending on the parametric gain G in the cases of constructive and destructive interference at the center of the beam. FWHM spatial profile width is FWHM = 170 μm, crystal length $L = 2$ mm, distance between crystals $d = 6$ mm, $\lambda_{\rm s} = \lambda_{\rm i} = 800$ nm, $\lambda_{\rm p} = 400$ nm.

significantly,

$$\chi_n(\theta_{\rm s}, \theta_{\rm i}) = (-1)^n I_n\left(\frac{\theta_{\rm s}\theta_{\rm i}}{a^2}\right) \exp\left(-\frac{\theta_{\rm s}^2+\theta_{\rm i}^2}{2a^2}\right)$$
$$\times \operatorname{sinc}\left(\frac{\theta_{\rm s}^2+\theta_{\rm i}^2}{b^2}\right) \cos\left(\frac{\theta_{\rm s}^2+\theta_{\rm i}^2}{b_1^2}+\alpha\right)$$
$$\times \exp\left[-{\rm i}\left(\frac{\theta_{\rm s}^2+\theta_{\rm i}^2}{b_2^2}+\alpha\right)\right], \qquad (47)$$

where $I_n(\xi)$ is the Infeld function.

The Schmidt decomposition of the bipartite function (47) gives a set of 'radial' modes for each azimuthal channel. Due to the smoothness of the Infeld function, the spatial distributions of photons in different azimuthal channels are very close to each other, which leads to a weak dependence of the 'radial' modes on the azimuthal channel number. Hence, channels with different OAM projections onto the z-axis have similar sets of radial modes. A noticeable difference arises for large numbers n, when the weight of a given channel is already negligible. An important feature of 'radial' Schmidt modes is their immense difference from the Laguerre–Gaussian modes that arise in the case of a single crystal, as is most pronounced in the case of interference suppression of the intensity at the beam center ($\alpha = \pi/2$), when all radial modes, including the zeroth-order one, are equal to zero at the specified point.

Let us discuss the behavior of weights and profiles of modes depending on the parametric gain and the distance between interferometer crystals. The characteristic distribution over azimuthal modes for a sufficiently small separation of the crystals is shown in Fig. 6a for two phase values, $\alpha = 0$ and $\pi/2$. It can be seen that, for interference suppression of the intensity at the beam center, the distribution over small-number azimuthal modes is flatter and smoother than for the zero phase. This difference might seem insignificant. However, as the parametric gain increases, for example, with increasing pump intensity, the mode distribution becomes sharper in both cases, and the effective number of modes decreases. In the zero-phase case, only one azimuthal mode with $n = 0$ survives at sufficiently strong pumping. At the same time, at $\alpha = \pi/2$, due to the initially flatter mode distribution, not one but several modes survive at high parametric gain, as shown in Fig. 6b. As regards the radial modes, their number also decreases as the pump intensity increases.

We analyze what happens as the separation of the crystals in the interferometer increases. The relative phase α of pumping and of the signal and idler radiation, occurring in (46) and (47), increases linearly upon increasing the crystal separation d, which leads to a periodically changing regime of constructive and destructive interference in the second crystal. In the degenerate case, the difference between the refractive indices in air for the pump and signal/idler photons is very small (of the order of 10^{-5}), but this is sufficient for a significant phase increase over an air gap several centimeters in length. As a consequence, as the crystal separation increases, the output intensity profiles change quasiperiodically from a localized beam with a maximum at the center to a broadened distribution with a central minimum. Accordingly, depending on the separation, the effective number of modes also changes, as is shown in Fig. 7 for azimuthal modes in the low and high parametric gain regimes.

As can be seen from Fig. 7, the initial number of modes is much smaller in the case of stronger pumping, and is of the order of unity when constructive interference is attained. Moreover, with a further increase in the distance between the crystals, the radiation of parametric scattering from the first crystal, entering the second crystal where it can be amplified, has a progressively smaller angular distribution width σ/d (where σ is the pumping diameter and d is the width of the air gap between the crystals). As soon as this value becomes of the order of the correlation width, only one mode is to be registered at the exit from the second crystal according to the Fedorov relation [64, 65].

The generation of a single spatial mode has been demonstrated experimentally, and good agreement with theoretical predictions was observed [108].

Figure 8 shows the angle-integrated intensity of the detected squeezed light and the magnitude of the second-order correlation function $g^{(2)}$ varying quasiperiodically with the separation of the crystals. For some separations, two-dimensional intensity distributions in the far zone are shown, demonstrating a significant change in the angular spectrum of the signal with increasing separation. Because a multimode spatially squeezed vacuum was generated in the experiment, the theoretical value of $g^{(2)}$ for the total signal can be

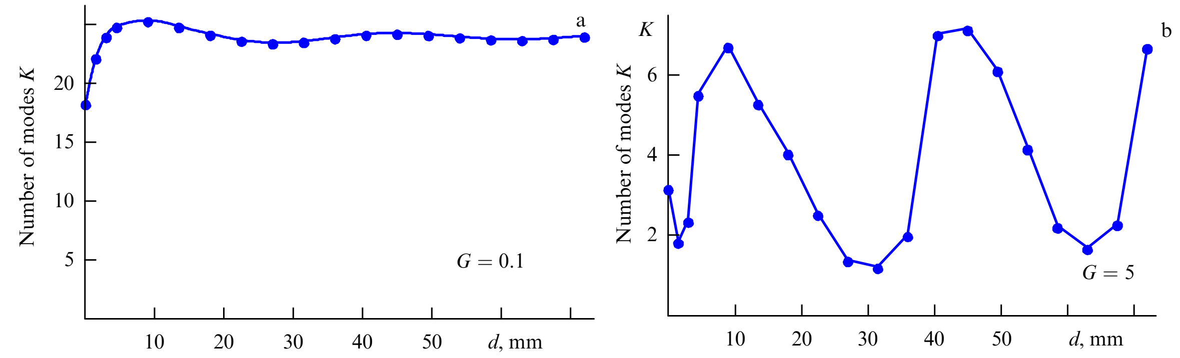

Figure 7. Dependence of the number of azimuthal modes on distance d between crystals for (a) small and (b) large parametric gain values. FWHM of the spatial pump profile is FWHM = 170 μm, crystal length $L = 2$ mm, $\lambda_s = \lambda_i = 800$ nm, $\lambda_p = 400$ nm.

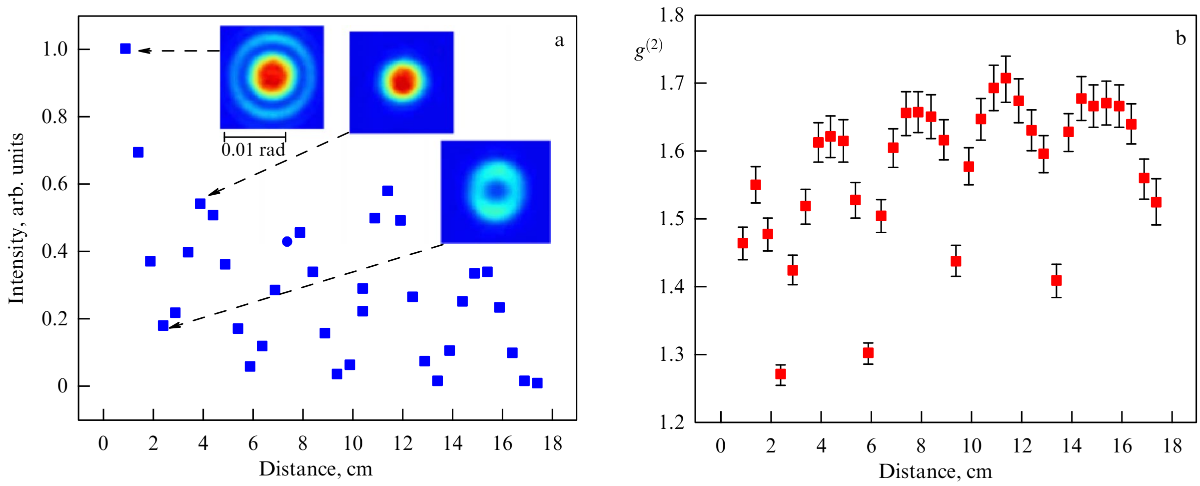

Figure 8. (a) Angle-integrated intensity of squeezed light and (b) second-order correlation function $g^{(2)}$ depending on the distance between crystals [108]. Crystal length is $L = 3$ mm, pump parameters are $\lambda_p = 355$ nm, FWHM = 200 μm, power is 60 mW, pulse duration is 18 ps.

calculated in terms of the correlation function of an individual mode $g_1^{(2)}$ and the number of modes m according to the formula [112]

$$g^{(2)} - 1 = \frac{g_1^{(2)} - 1}{m} \,. \tag{48}$$

A second-order autocorrelation function used in experiment can be calculated for each twin beam generated in one spatial Schmidt mode as $g_1^{(2)} = \langle N_s^2 \rangle / \langle N_s \rangle^2$. Using the solutions found in (17), it can be shown that $g_1^{(2)} = 2$. It hence follows from (48) that $g^{(2)}$ reaches a maximum, equal to 2, in the case of one mode. With the 1.25 frequency modes observed in the experiment, the theoretical estimate of $g^{(2)}$ becomes less than 2 and nearly coincides with the maximum measured value of $g^{(2)}$ in Fig. 8b. Using the maximum value of $g^{(2)}$ obtained in the experiment and taking the correction for the number of frequency modes into account, the estimate of the number of spatial modes by formula (48) gives the value $m = 1.1$. Thus, the generation of a squeezed vacuum in the 1.1 spatial mode was implemented experimentally.

However, one mode is not always selected. It has been found that, at large distances between crystals, the mode structure changes due to the strong interference-induced 'roughness' of the two-photon amplitude [101].

In this regime, radial modes can be found analytically as the product of a single crystal mode and an oscillating factor represented as a sine or cosine [101],

$$\begin{aligned} u_{n,p}^{(1)}(\theta_{s,i}) &\sim u_{n,p}^{(0)}(\theta_{s,i}) \cos\left(\frac{\theta_{s,i}^2}{2b_2^2} + \frac{\alpha}{2}\right), \\ u_{n,p}^{(2)}(\theta_{s,i}) &\sim u_{n,p}^{(0)}(\theta_{s,i}) \sin\left(\frac{\theta_{s,i}^2}{2b_2^2} + \frac{\alpha}{2}\right), \end{aligned} \tag{49}$$

where the parameter b_2, defined in (46), bears an essential dependence on the distance between the crystals.

In the limit of a large distance between crystals, these modes have the same weights. Figure 9 shows the radial mode distribution for the zero azimuthal channel when weight 'doubling' is just starting.

Due to the presence of 'double' modes, even in the limit of strong pumping, at least two radial modes remain at long distances between the crystals; singling out one mode is not possible. This effect also manifested itself in the experiment in [108] as a decrease in the measured second-order correlation function in the limit of large separations of the crystals.

Thus, the scheme involving a nonlinear interferometer allows controlling the mode composition and the type of Schmidt modes. The approach outlined above opens up the possibility of creating a spatially single-mode field source in a squeezed vacuum state with all the properties of such a field preserved, which is an urgent task for various practical applications but is extremely difficult to implement by

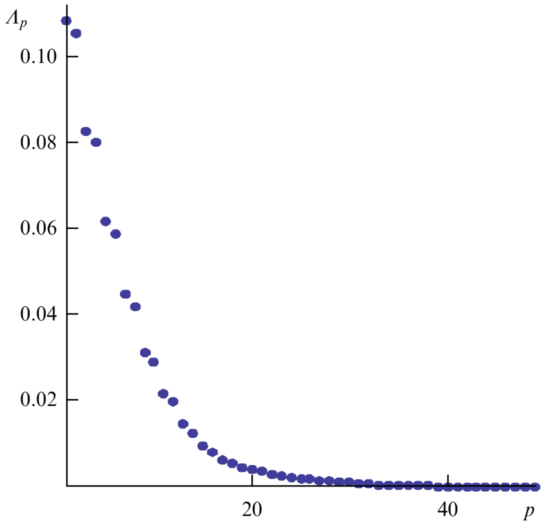

Figure 9. Radial mode distribution of a squeezed vacuum at the exit from a nonlinear interferometer for the zero azimuthal channel at the stage of dual mode formation in the case of weak parametric gain. Length of crystals is $L = 2$ mm, distance between crystals is $d = 72$ mm.

standard filtering methods due to the significant destruction of nonclassical properties and photon correlations of squeezed light.

3.3 Spatial photon correlations

As discussed in Section 3.2, the squared modulus of the biphoton amplitude characterizes the mutual spatial distributions and correlations of photons in the case of weak pumping (low parametric gain). Photon correlations, which are the most important property of a squeezed vacuum, manifest themselves in terms of spatial, frequency, and quadrature variables. One of the quantitative characteristics of the spatial correlations of photons in the case of an arbitrary parametric gain is the covariance of the spatial intensity distributions, which can be measured experimentally. Although this quantity does not carry information about phase correlations, it allows finding correlations of the intensities of the generated squeezed vacuum at different spatial points. The general expression for the covariance of the angular intensity distributions measured in the far zone for the angles (θ_1, ϕ_1) and (θ_2, ϕ_2) or the transverse wave vector components q_1 and q_2 has the form

$$\operatorname{cov}(q_1, q_2) = \operatorname{cov}\left[I(q_1),\, I(q_2)\right] = \left\langle I(\mathbf{q}_1)\, I(\mathbf{q}_2)\right\rangle - \left\langle I(\mathbf{q}_1)\right\rangle\left\langle I(\mathbf{q}_2)\right\rangle . \tag{50}$$

Because both signal and idler photons can contribute to the intensity of the output field for each direction q, expression (50) can be divided into several terms [93, 113]:

$$\operatorname{cov}(q_1, q_2) = \operatorname{cov}\left[I_{\rm s}(q_1),\, I_{\rm s}(q_2)\right] + \operatorname{cov}\left[I_{\rm i}(q_1),\, I_{\rm i}(q_2)\right] + 2\operatorname{cov}\left[I_{\rm s}(q_1),\, I_{\rm i}(q_2)\right] . \tag{51}$$

The first two terms on the right-hand side of (51) correspond to so-called autocovariance, i.e., covariance of the field intensity of only signal or only idler photons at different points, while the second term describes twice the cross-covariance of the field intensities of signal and idler photons. Using the introduced Schmidt modes, we can obtain the following expressions for auto- and cross-covariance [101, 113]:

$$\begin{aligned} \operatorname{cov}(\mathbf{q}_1, \mathbf{q}_2)_{\rm auto} &= \left| \sum_{n,p} \frac{u_{n,p}(q_1)\, u^*_{n,p}(q_2)}{\sqrt{q_1 q_2}} \sinh^2\left(G\sqrt{\lambda_{n,p}}\right) \times \exp\left[{\rm i}n\,(\phi_1 - \phi_2)\right] \right|^2 , \\ \operatorname{cov}(\mathbf{q}_1, \mathbf{q}_2)_{\rm cross} &= \left| \sum_{n,p} \frac{u_{n,p}(q_1)\, v_{n,p}(q_2)}{\sqrt{q_1 q_2}} \sinh\left(G\sqrt{\lambda_{n,p}}\right) \times \cosh\left(G\sqrt{\lambda_{n,p}}\right) \exp\left[{\rm i}n\,(\phi_1 - \phi_2)\right] \right|^2 . \end{aligned} \tag{52}$$

For low parametric gain, the spatial distribution of the cross-covariance coincides with the distribution of the squared biphoton amplitude modulus (Fig. 5a, c). For high parametric gain, the form of the covariance changes. Because the lowest radial mode starts dominating in that case, the distribution corresponding to the covariance is localized, taking the form of a small circle located at the center in the case of constructive interference ($\alpha = 0$) or away from the center for $\alpha = \pi/2$ (destructive interference regime). This is true for the covariance of both signal and idler photons (cross-covariance) and photons in one beam (autocovariance).

Thus, for any values of the parametric gain coefficient, the cross-covariance reaches a maximum when the azimuthal angles of the photon wave vectors differ by π, and hence the distribution shown in Fig. 3b is also valid for arbitrary values of the parametric gain. However, it was found that, as the pump intensity increases, the width of the distribution increases and its maximum height decreases [101]. Therefore, as the parametric gain increases, the characteristic width of the correlations increases. A feature of autocovariance is that it attains a maximum when the azimuthal angles of the photon wave vectors coincide.

In Fig. 10a, we show the measured covariance as a function of the external polar angles of photons [93]. Almost completely symmetric distributions along the main diagonal correspond to the cross-covariance; the autocovariance distributions are rotated by 90°.

Thus, when there is intense pumping into essentially a single spatial mode due to the generation of a squeezed vacuum, photon correlation occurs for a specific value of the polar angle and opposite azimuthal angles, i.e., for certain directions of photon wave vectors.

We note that covariance can be used not only to extract information about photon correlations but also to obtain Schmidt mode profiles.

In experiment, it is difficult to measure the shape of the modes directly, but their reconstruction from the covariances can be attempted. It was shown in [101] that, in the far zone, the dependence of the phases on $q_{\rm s,i}$ is the same for all $u_{n,p}$ modes. This allows reconstructing the far-field modes by taking the square root of the covariance and performing the Schmidt decomposition for the resulting function; the true mode weights must then be adjusted using formulas (52).

The spatial modes reconstructed theoretically from covariance in the framework of this approach are identical to the Schmidt modes for the biphoton amplitude at any parametric gain (although the shape of the covariance changes with the gain). A similar procedure was implemented in an experiment

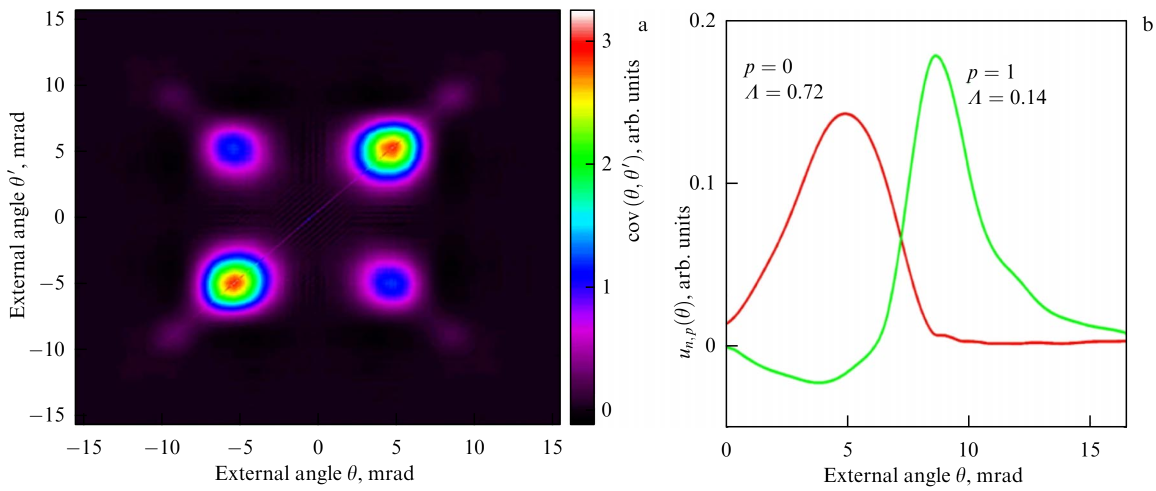

Figure 10. Measured (a) covariance and (b) profiles and weights reconstructed from it for the two lowest dominant radial Schmidt modes [93]. Crystal length is $L = 2$ mm, distance between them $d = 15$ mm, pump parameters are $\lambda_{\mathrm{p}} = 354.67$ nm, FWHM $= 170$ μm, and power 45 mW. To obtain profiles and weights, integration over the 9° azimuthal angle was carried out.

where the reconstruction accuracy turned out to also be quite high [93, 113]. The reconstructed profiles for the two dominant modes are shown in Fig. 10b [93].

Thus, covariances allow theoretically predicting and experimentally measuring the spatial correlations of photons, as well as obtaining information about the profiles and weights of Schmidt modes.

3.4 Photon correlations in the angular momentum projection

As shown in Section 3.1 (and in discussing Fig. 3), signal and idler photons are strongly correlated in the azimuthal angle and therefore have opposite transverse wave vectors. It follows from decomposition (11) that conjugate-mode photons have opposite values of the azimuthal quantum numbers (topological charge) $(+n)$ and $(-n)$; in other words, there is a correlation of photons with opposite angular momentum projections on the z-axis for all azimuthal modes, except the one with $n = 0$.

Correlated photons were experimentally selected in conjugate azimuthal modes in the multiphoton regime of four-wave mixing by illuminating one of the conjugate channels by the Laguerre–Gaussian mode with a fixed angular momentum projection [114]. If the pumping also has a nonzero OAM, then correlations between photons arise in azimuthal modes with angular momentum projections differing in absolute value but satisfying the conservation law with the pumping OAM taken into account [114, 115]. We note that this scheme selects only a pair of conjugate modes correlated in the number of photons and quadrature entanglement, but strong spatial entanglement is not achieved.

Sorting the modes by states with different OAM projections was implemented in [116] based on optical elements that convert a twisted phase front of the beam in a polar coordinate system into a transverse phase gradient in a Cartesian system. It was thus possible to spatially separate 11 states with different OAM projections. In this case, however, the zero mode partially overlaps with the neighboring modes, which can drastically reduce photon correlations in conjugate modes and increase the NRF. Because photons with zero OAM are not correlated with photons of other modes, the prevailing population of the zero orbital channel strongly suppresses photon correlations in the OAM projection, or so-called azimuthal entanglement. An important task in the multimode case is therefore to suppress the signal in the zero azimuth channel without introducing additional noise.

The problem is that, even in the case of parametric generation of squeezed light in the far field of a nonlinear interferometer, different azimuthal modes share similar spatial distributions [101], which makes it extremely difficult to select different azimuthal channels. But in the near field, as shown in [117], different orbital channels have different spatial localization: photons corresponding to different azimuthal modes are produced in different regions of the crystal. Moreover, modes with zero OAM are mainly localized in the center of the beam, while those with a large OAM reside farther from the center. Thus, it becomes possible to select modes with different orbital angular momenta. Still, achieving the complete separation of the channels is impossible due to a partial overlap of the localization zones. To suppress the zero channel, a 'mask' can be installed to block the zero channel in the near zone. Because this would introduce noise and somewhat deteriorate the nonclassical properties in other modes, the transmitted modes with a nonzero OAM would have to be amplified in the second crystal. An alternative approach can be to use a near-field diaphragm that is maximally transparent to the zero-mode signal, which should then be suppressed in the second system of crystals due to the effect of destructive interference when the relative phase changes by π.

As it turns out, the suppression of the zero channel by a mask is preferable. Moreover, selecting the mask size and the parametric gain in the first and second crystals (G_0 and G, respectively) allows selecting the azimuthal channel with a certain OAM projection on the z-axis whenever necessary. We note that a more efficient suppression of the zero azimuthal channel can be achieved if each of the two nonlinear crystals is replaced with a nonlinear interferometer phase-shifted by $\pi/2$, as described in Section 3.2. Then, with the intensity suppression at the beam center due to interference, the distribution over small-number azimuthal modes becomes flatter and the relative contribution of the zero mode does not become too prominent (see Fig. 6). Moreover, this mode provides a maximum difference between spatial localizations of different azimuthal channels.

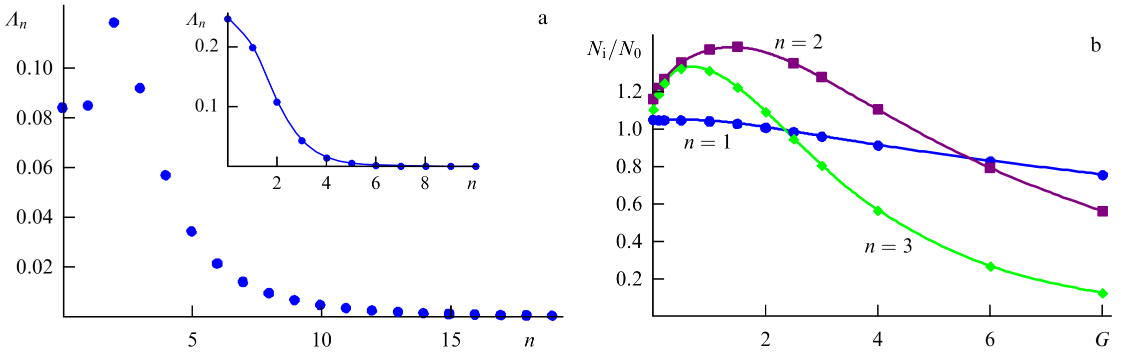

Figure 11. Suppression of the zero mode and amplification of the azimuthal channel with $n = 2$ using a mask with a diameter of 350 pump wavelengths. (a) Redistribution of mode weights for parametric gain with $G = 1.5$; inset shows initial distribution over azimuthal modes. (b) Number of photons in the $n = 1, 2, 3$ modes relative to the contribution of the zero mode as a function of parametric gain G. Interferometer parameters are the same as in Fig. 5.

In Fig. 11, we show the result of zero mode suppression and the $n = 2$ azimuthal channel amplification using a mask. Depending on the parametric gain G in the second crystal, we can obtain a different ratio of the weights of the azimuthal modes at the exit. In particular, at $G = 1.5$, the signal from the azimuthal mode with $n = 2$ is clearly dominant. The redistribution of the azimuthal mode weights in this case is shown in Fig. 11a. A significant change in the fraction of the number of photons in modes with $n = 1, 2, 3$ compared with the zero mode, depending on the parametric gain coefficient, as shown in Fig. 11b, suggests the possibility of varying the pump intensity to choose the regime where one Schmidt mode or another is dominant. Thus, in an essentially multimode regime, the described scheme allows not only suppressing the signal in the zero mode while preserving the photon correlations but also changing the relative weights of the azimuthal modes.

An important aspect of the considered mode selection process is the preservation of photon correlations. To characterize the correlations in this case, it is convenient to use the NRF in Eqn (27), which is proportional to the variance of the difference between the numbers of photons in the signal and idler beams. A significant contribution to this variance is made by the number of photons in the zero azimuthal mode. That is why the suppression of the signal with $n = 0$ is of fundamental importance for the preservation of photon correlations. It is difficult, but quite possible, to simultaneously satisfy the conditions for optimal selection of azimuthal modes and preserve the photon correlations (NRF $\ll 1$).

4. Parametric scattering in a strongly frequency-nondegenerate regime

The effects described in Section 3 relate to parametric generation in the frequency-degenerate regime. In the case of a nondegenerate regime, a number of features arise, the most interesting and promising of which from the standpoint of practical applications is the generation of squeezed light that is strongly nondegenerate in frequency when the frequency of signal photons lies in the optical region and idler photons correspond to the THz frequency range. Here, the idler photon frequency approaches the phonon excitation frequencies, and parametric scattering acquires the features of light scattering on polaritons [1]. In fact, there are medium states 'dressed' by the acting field, and partial absorption of the idler wave occurs.

A strongly frequency-nondegenerate regime of parametric scattering was observed in lithium niobate crystals [118–122]. Based on study [123], experimental methods were developed in [124–126] for measuring the brightness and for calibrating detectors in the THz frequency range. The theoretical analysis of highly frequency-nondegenerate parametric scattering is a difficult task, because it is often necessary to take the absorption and the effect of thermal noise for the THz channel into account. Most of the theoretical work is based on solving Maxwell's equations for classical fields or finding the evolution of plane-wave photon creation/annihilation operators, because this approach occasionally allows taking absorption into account [127–130]. However, for negligibly small absorption (not very low idler photon frequencies), optical-THz squeezed light can be described using a theoretical approach in the formalism of Schmidt modes and operators, similar to that considered in Section 2.2 but generalized for the case of significantly different frequencies of the signal and idler photons [131, 132].

4.1 Generation of nonclassical THz radiation in a single crystal

We analyze the highly nondegenerate regime of generation and the spatial properties of the generated optical-THz squeezed light in the formalism of Schmidt modes and operators. For a single crystal and a Gaussian spatial shape of pumping, this process is described by Hamiltonian (4) with a biphoton amplitude that can be approximately represented as

$$F(\mathbf{q}_s, \mathbf{q}_i) = C \exp\left[-\frac{(\mathbf{q}_s + \mathbf{q}_i)^2 \sigma^2}{2}\right] \operatorname{sinc}\left(\frac{\Delta k_{\parallel} L}{2}\right) \times \exp\left(-\mathrm{i}\,\frac{\Delta k_{\parallel} L}{2}\right), \tag{53}$$

where $\Delta k_{\parallel}$ is the longitudinal mismatch of the wave vectors of the pump, signal, and idler photons, which can be calculated as

$$\Delta k_{\parallel} = \sqrt{k_p^2 - (\mathbf{q}_s + \mathbf{q}_i)^2} - \sqrt{k_s^2 - q_s^2} - \sqrt{k_i^2 - q_i^2}\,. \tag{54}$$

We note that, due to the considerable difference between the frequencies of the signal and idler photons in (54), it is impossible to use the approximation based on the smallness of the transverse components of the wave vectors, which leads to a simplified form of the longitudinal detuning in the degenerate collinear mode (5), because the phase matching condition corresponds to the opposite transverse wave

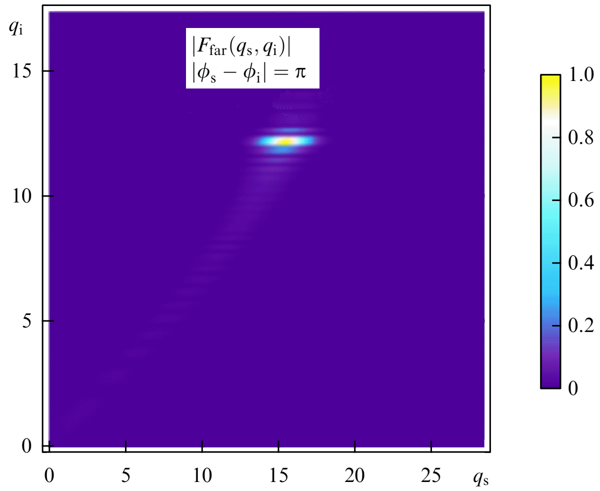

Figure 12. Biphoton amplitude modulus normalized to the maximum, depending on transverse components of wave vectors of signal (optical) and idler (THz) photons at the maximum correlation in azimuthal angles $\phi_s - \phi_i = \pi$ [131]. $L = 10$ mm, $\sigma = 1$ mm, $\lambda_p = 514.5$ nm, $n_s = 2.33$, $n_i = 5.102 - 0.0473\nu + 0.05887\nu^2$, with $\nu = 0.16$ THz the idler photon frequency.

vectors of the signal and idler photons:

$$\mathbf{q} = \mathbf{q}_s = -\mathbf{q}_i \,. \tag{55}$$

The phase-matching condition in a highly nondegenerate regime can only be satisfied for a THz photon with the wave vector modulus q determined by the refractive indices at the optical and THz frequencies:

$$q = k_i \sqrt{1 - \frac{n^2(\omega_p)}{n^2(\omega_i)}} \,. \tag{56}$$

In Fig. 12, we show the biphoton amplitude modulus normalized to the maximum. As can be seen, the spread in transverse wave vectors is noticeably larger for optical photons. But the picture changes dramatically when converted into polar angles of photons inside the crystal,

$$\begin{aligned} \theta_s &= \frac{q}{k_s} \approx \frac{k_i}{k_p} \sqrt{1 - \frac{n_p^2}{n_i^2(\omega_i)}} \,, \\ \sin\theta_i &= \frac{q}{k_i} \approx \sqrt{1 - \frac{n_p^2}{n_i^2(\omega_i)}} \,; \end{aligned} \tag{57}$$

due to the significant difference in frequencies, the characteristic polar angle of the wave vector of optical photons is very small, and the radiation is directed almost parallel to the pumping, while the THz radiation is characterized by angles inside the crystal of the order of 60° with a width of at least 10° [131, 132]. Such values of internal angles allow THz radiation to escape from the crystal due to total internal reflection. Only by supplementing the crystal with a prism of a particular shape and refractive index can THz radiation still be extracted, but it would have a large angular aperture, entailing great difficulties in detecting the complete THz signal. These features of the spatial distribution of low-frequency THz radiation generated at the difference frequency were initially analyzed for classical fields in [133].

To analyze the spatial properties of optical-THz squeezed light, it is convenient to use the Schmidt mode formalism. In accordance with the technique described in Section 2.2, two-photon amplitude (53) can be decomposed with respect to azimuthal channels. Due to the smallness of the radiation frequency and the spread of transverse wave vectors of THz photons compared to optical ones, and also due to the large pump width (about 1 mm), the angular distributions in different azimuthal channels are very close to each other and actually correspond to the distribution for the two-photon amplitude shown in Fig. 12 [131, 132]. Moreover, the distribution for each OAM channel actually factors into the product of two dominant radial modes for the signal and idler channels, whose profiles can be found analytically as

$$\begin{aligned} u(q_s) &= N_u \sqrt{q_s} \exp\left(-\frac{\Delta q_s^2 \sigma^2}{2}\right) \exp\left(-\mathrm{i}\,\frac{\Delta q_s q L}{\kappa_s}\right), \\ v(q_i) &= N_v \sqrt{q_i}\, \operatorname{sinc}\left(\frac{\Delta q_i q L}{\kappa_i}\right) \exp\left(-\mathrm{i}\,\frac{\Delta q_i q L}{\kappa_i}\right), \end{aligned} \tag{58}$$

where $\kappa_s = \sqrt{k_s^2 - q_s^2}$ and $\kappa_i = \sqrt{k_i^2 - q_i^2}$. The dominance of a single radial mode for each of the conjugate beams naturally follows from the shape of the distribution in Fig. 12, showing a slight change in values when one of the arguments is fixed.

Thus, the Schmidt-mode photon operators evolve as described in Section 2.2, but the weights and mode profiles differ significantly from those in the case of identical photon frequencies.

The presence of a single radial mode means that there is no entanglement of photons in the polar angle and that the angular distribution of the intensity of the generated optical and THz radiation cannot be changed significantly. At the same time, there are a sufficiently large number of azimuthal modes, which depends significantly on the frequency of idler photons. Figure 13 shows how the probability density of the signal and idler photons depends on the difference between their azimuthal angles. It can be seen that, similarly to the degenerate regime, the photons are maximally correlated at the angular difference $\phi_s - \phi_i = \pi$. However, the distribution width significantly depends on the idler photon frequency and increases as the frequency decreases to values below 1 THz. The effective number of azimuthal modes decreases with increasing distribution width. Thus, the number of azimuthal modes increases with an increase in the frequency of THz photons, and the degree of azimuthal entanglement therefore increases.

We note that a number of important properties found in the case of identical photon frequencies and discussed in Sections 2 and 3 are preserved in the strongly nondegenerate regime of parametric scattering. First and foremost are the strong correlations for photons with opposite azimuthal angles and opposite OAM projections. There is also a two-mode quadrature squeezing, the operator of the difference between the number of photons in conjugate channels being an integral of motion (ignoring absorption). However, special features arise due to the presence of thermal noise in the THz mode. Because the variance of the photon number difference in the coupled channels remains equal to its value at the entrance to the crystal, we can represent the theoretical expression for the NRF in Eqn (27) in the case of one dominant mode for each of the coupled channels in the form

$$\mathrm{NRF} = \frac{D_{N_s} + D_{N_i}}{N_s + N_i + 2(N_s + N_i + 1)\sinh^2 G} \,, \tag{59}$$

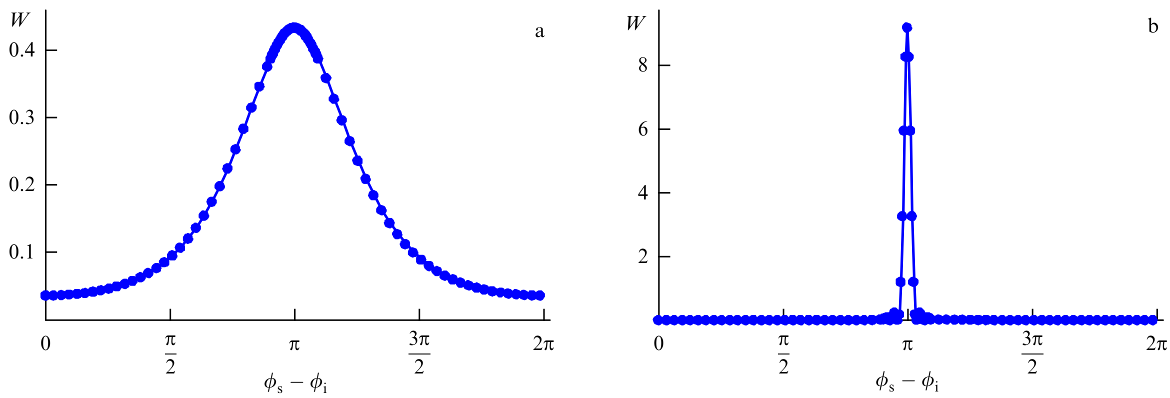

Figure 13. Correlation of optical and THz photons in the azimuthal angle at THz photon frequency (a) $\nu = 0.05$ THz and (b) $\nu = 0.5$ THz [132]. Parameters are the same as in Fig. 12.

where $D_{N_s} + D_{N_i}$ is the sum of variances of the number of photons of the signal and idler modes at the entrance to the crystal, $N_s + N_i$ is the sum of the mean numbers of photons of these modes at the entrance to the crystal, and G is the parametric gain factor. If the signal and idler modes are initially in the vacuum state, then the zero numerator in (59) leads to the minimum theoretical value NRF $= 0$. But in the case of thermal radiation at the entrance to the crystal, a nonzero variance in the number of photons arises for the THz mode, which in the spontaneous regime with low parametric gain can lead to suppression of the intensity correlation in the modes due to the smallness of the function $\sinh G$ in the denominator of (59). Thus, there is a theoretical bound on the NRF value from below, determined by the smallness of the parametric gain and the temperature of the medium.

4.2 Advantages of the scheme with a nonlinear interferometer

As shown in Section 4.1, the spatial distribution of the optical-THz squeezed vacuum is actually determined by a single radial mode dominant in each channel. Therefore, the task of developing methods for controlling the mode composition for such fields is particularly acute. One of the solutions is to use a nonlinear Mach–Zehnder interferometer, discussed in Section 3. The most convenient scheme is with a linear dispersion in the intermediate layer. The optical THz fields generated in the first crystal are then amplified or attenuated in the second crystal, depending on their phase with respect to the pumping, realizing a spatial analogue of Ramsey interference. The Ramsey time-frequency interference effects in spontaneous parametric scattering were discussed in [134]. For the arrangement with an interferometer in the frequency-nondegenerate regime, the biphoton amplitude is given by [132]

$$F(\mathbf{q}_s, \mathbf{q}_i) = C \exp\left(-\frac{\sigma^2(\mathbf{q}_s + \mathbf{q}_i)^2}{2}\right) \operatorname{sinc}\frac{\Delta k_{||} L}{2} \times \cos\left(\frac{\Delta k_{||} L + \Delta k_{\mathrm{d}||} d}{2}\right) \exp\left[-\mathrm{i}\left(\Delta k_{||} L + \frac{\Delta k_{\mathrm{d}||} d}{2}\right)\right], \tag{60}$$

where $\Delta k_{||} = k_{\mathrm{pe}} - (k_{\mathrm{se}}^2 - q_s^2)^{1/2} - (k_{\mathrm{ie}}^2 - q_i^2)^{1/2}$, $\Delta k_{\mathrm{d}||} = k_{\mathrm{po}} - (k_{\mathrm{so}}^2 - q_s^2)^{1/2} - (k_{\mathrm{io}}^2 - q_i^2)^{1/2}$ are the respective longitudinal mismatches of the wave vectors of the pump, optical, and THz photons in the crystal and in the medium with the relation $k = n\omega/c$ taken into account, L is the length of each crystal, d is the distance between them, and the subscripts e and o mark the extraordinary and ordinary rays in the crystal and the intermediate layer. We note that expression (60) is similar to (45) but is more general, because it involves no approximations in calculating the longitudinal mismatches. Interference effects lead to the appearance of maxima and minima in the distribution of idler and signal photons over transverse wave vectors (Fig. 14). Their position and number are determined by phase shifts and dispersion in the medium, which depend on the frequency of THz photons and are determined by the condition $\Delta k_{||} L + \Delta k_{\mathrm{d}||} d \approx 2\pi m$.

It then follows that the weights and profiles of the Schmidt modes change. In addition to azimuthal modes, a set of 'radial' modes appears, which significantly increase the degree of spatial entanglement of optical and THz photons. The frequency-angular spectrum for the scheme with an interferometer differs significantly from that in the case of a single crystal (Fig. 15). For parameters close to the experimental conditions in [132], in the low-gain regime, the distribution of photons over transverse wave vectors, which is determined under these conditions by the squared modulus of the biphoton amplitude, acquires either one main maximum or two secondary maxima (Fig. 14b). As a result, the frequency-angular spectrum has the shape shown in Fig. 15b.

An entirely different picture is realized at high values of the parametric conversion coefficient. Due to the nonlinear amplification, the single main maxima start dominating, and double maxima in the frequency-angle spectrum are superseded by troughs. Thus, THz photons are emitted predominantly at certain frequencies, and their interference is suppressed at frequencies corresponding to the minima (Fig. 15c).

The detected interference effects are significantly affected by the dispersion of THz radiation in the intermediate layer. This fact can be used to accurately find the unknown dispersion properties of various media in the THz frequency range, which is an important and needed task, based on measurements of the frequency-angle spectrum in the optical range. The advantage of this approach is that, although the measurements are carried out in the optical channel, photon correlations yield information about the medium properties in the THz frequency range. Initially, this idea was developed theoretically and implemented experimentally for idler photon frequencies in the infrared (IR) range [135]. Later, the same method was applied to IR spectroscopy of molecules in optical range measurements based on photon correlations in conjugate modes [136].

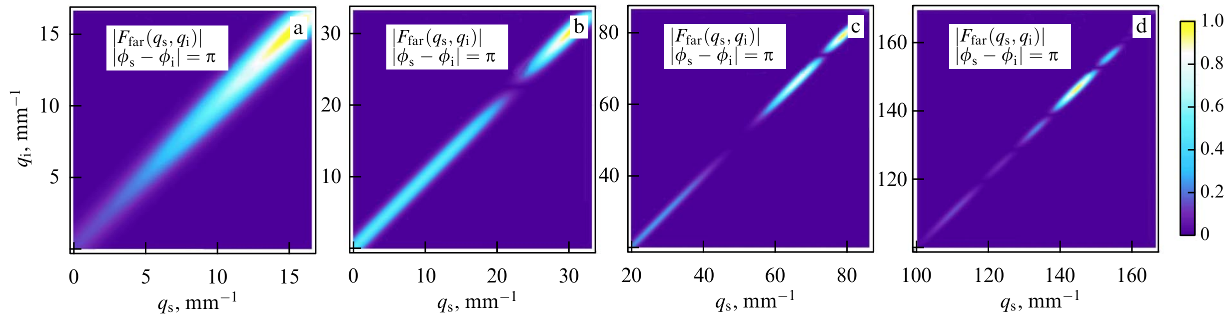

Figure 14. Absolute value of biphoton amplitude (60) depending on the transverse wave vectors of signal and idler photons in the case of maximum correlation in the azimuthal angle: (a) $\omega_i = 10^{12}$ s^{-1}, (b) $\omega_i = 2 \times 10^{12}$ s^{-1}, (c) $\omega_i = 5 \times 10^{12}$ s^{-1}, (d) $\omega_i = 10^{13}$ s^{-1} [132]. Pump wavelength $\lambda_p = 514.5$ nm, crystal length $L = 0.235$ mm, intermediate layer thickness $d = 0.085$ mm.

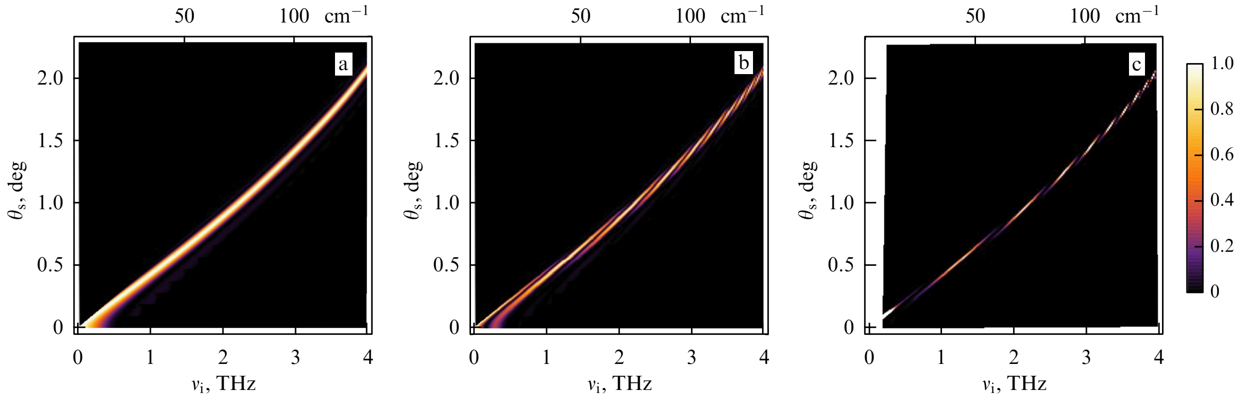

Figure 15. Frequency–angle spectrum calculated (a) for one crystal and for the scheme with an interferometer in (b) low, $G = 0.1$, and (c) high, $G = 5$, parametric gain regimes. Crystal length $L = 0.235$ mm, intermediate layer thickness $d = 0.085$ mm.

In [132], the refractive index of the medium in the intermediate layer of the interferometer was calculated theoretically and measured experimentally in the THz frequency range. Based on the interference character of the expression for the biphoton amplitude, Eqn (60), the accuracy of determining the refractive index was estimated to be no worse than

$$\Delta n = \frac{\pi c}{2\omega_i d}\,. \tag{61}$$

In fact, for the parameter values $d = 2.5$ mm and $\nu_i = 1.5$ THz, the accuracy $\Delta n \sim 0.05$ can be achieved. Large thicknesses of the intermediate layer turn out to be critical as regards increasing the absorption of THz radiation. A significant decrease in the thickness of the measured medium significantly reduces the measurement accuracy. In the experiment in [132], the intermediate layer with a thickness of about 0.1 mm was used, and therefore the accuracy of measuring the refractive index did not exceed 0.2. Nevertheless, the experiment demonstrated for the first time the possibility of such a measurement in the THz frequency range.

Another advantage of the interferometer scheme is the ability to vary the mode composition and then amplify a certain Schmidt mode and thus control the spatial distribution of the output squeezed light. The possibility of such control is especially important for THz radiation because its faultless detection requires generation in a narrower angular range, which can be realized by amplifying a certain THz mode with a narrower angular distribution. The most convenient way to do this is by seeding the conjugate optical mode, for example, with intense coherent light. By choosing the spatial profile of the optical seed so as to ensure a significant overlap with the mode most narrowly localized in polar angles, it is also possible to significantly amplify the signal in the conjugate THz mode. However, this is difficult to do for a single crystal of a large length because, as shown above, only one radial mode, the one that determines the distribution of outgoing photons over the polar angle, makes an effective contribution in the strongly nondegenerate frequency regime for one crystal, while the contribution of the remaining modes is negligibly small. For an interferometer, there are more radial modes with different polar angle localizations.

In Fig. 16, we show the spatial distributions of photons in the THz mode for a long crystal and in the setup involving an interferometer without and with the seeding of the optical channel by coherent light prepared in a superposition of Laguerre–Gaussian spatial modes with the azimuthal quantum numbers $n = \pm 3$. As can be seen, the intensity distribution of THz radiation for one crystal is predominantly characterized by internal polar angles (57) in the range of 50–60°. Even with the seeding, large values of the wave vector polar angles of THz photons cannot be effectively reduced, and the proportion of photons with small transverse wave vectors is negligible (Fig. 16b). With the interferometer, due to the richer mode composition, there are rather narrow modes of the optical channel that overlap well with seeded. Due to high-intensity seeding, they can be amplified. As a consequence, THz radiation is also predominantly amplified in the spatial mode coupled to the 'seeded' optical spatial mode. Figure 16d clearly shows

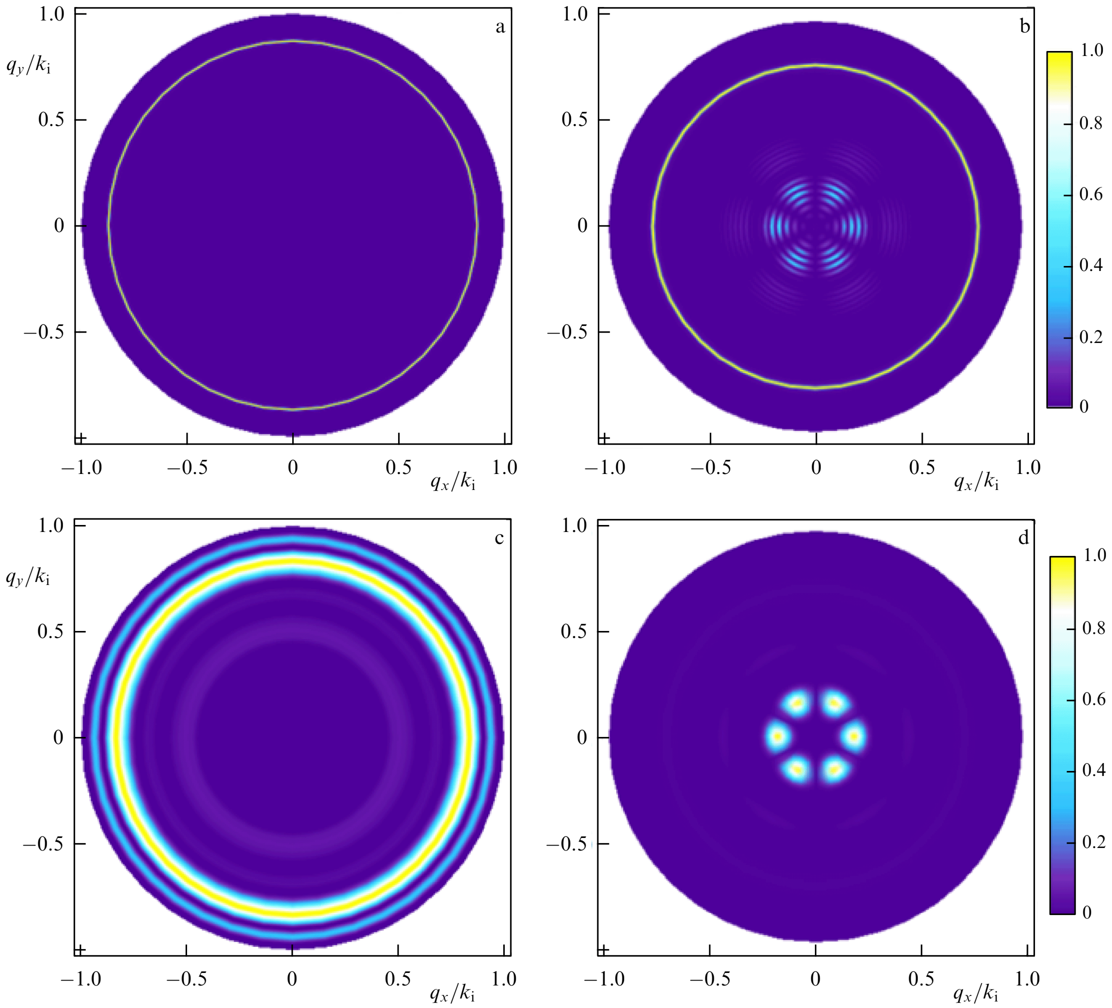

Figure 16. Distribution of THz photons depending on the transverse wave vector components: (a, b) in a single crystal ($L = 5$ mm) and (c, d) in an interferometer made of two crystals ($L = 0.25$ mm, $d = 0.087$ mm), (a, c) without seeding and (b, d) with seeding of the optical channel by Laguerre–Gaussian modes with $n = \pm 3$. Parametric gain $G = 1$.

the narrowing of the angular distribution of THz radiation amplified by seeding in the optical channel. In this case, characteristic values of internal polar angles of the order of 12° can be obtained for the THz mode [132]. The characteristic 'leafed' structure of the spatial distribution of THz photons due to the superposition of azimuthal modes with quantum numbers $n = \pm 3$ demonstrates the possibility of varying the spatial output intensity profile by amplifying certain azimuthal modes.

We note that, in this case, it is necessary to localize the optical illumination mode in the range of polar angles of the order of $\Theta \approx 0.01°$, which is a difficult task. However, this method allows selecting one or several narrow-angle Schmidt modes with small weights and localizing THz radiation within small polar angles without loss of correlations with optical photons in the signal beam.

Although the seeding of one of the channels changes the photon statistics of the generated squeezed optical-THz field, the correlations in the number of photons can be preserved. Under these conditions, the NRF that can be found theoretically from (59) can be much less than unity for illumination in a coherent state at a sufficiently high parametric gain.

4.3 Mutual influence of the difference and sum frequency generation processes

Another feature of parametric scattering in the nondegenerate regime is that, along with frequency down-conversion, up-conversion is also possible. This process consists in the fact that, in a medium with a quadratic nonlinearity, a pump photon and a THz photon give rise to a photon of the sum frequency. Such a process can be interpreted as sum frequency generation. In parametric scattering, in turn, optical photons of the difference frequency are generated that differ from the pump photon in energy by the THz radiation quantum. We note that the sum frequency is not generated in the absence of THz photons, but these can be produced in the course of frequency down-conversion. Because THz photons are involved in both processes, it is appropriate to consider the difference and sum frequency generation not separately but within a single approach. Double phase matching for both processes is observed quite rarely, but generation also occurs in the absence of phase matching for one of them [1]. A detailed analysis of the efficiency of cascade hyperparametric scattering depending on the phase matching conditions for each of the processes carried out in [137] showed that parametric amplification requires the phase matching conditions to be satisfied not for

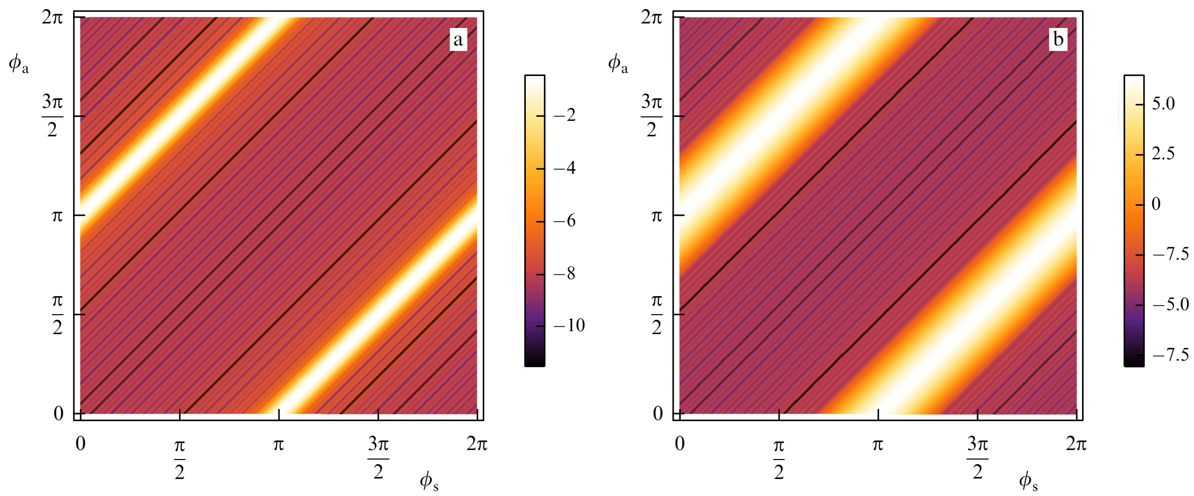

Figure 17. Covariance (65) depending on the azimuthal angles of Stokes and anti-Stokes photons in the case of (a) low, $G = 0.1$, and (b) high, $G = 5$, parametric gain [131]. Parameters are the same as in Fig. 12.

each of the processes separately but for the cascade process as a whole. The possibility of simultaneously realizing both noted nonlinear optical processes in a crystal with a periodic nonlinear inhomogeneity was previously demonstrated in [138, 139]. The mutual influence of the processes of generation of sum and difference frequencies in a strongly frequency-nondegenerate regime was studied in [131] using the formalism of Schmidt modes. Because the THz radiation Schmidt modes are the same in the case of difference and sum frequency generation, THz radiation can be characterized by the same operators in the Schmidt modes in both processes. The Hamiltonian describing simultaneous generation of the difference and sum frequencies has the form [131]

$$H = i\hbar\Gamma_1 \sum_{n,p} \sqrt{\lambda_{n,p}}\,(D^{\dagger}_{n,p}B^{\dagger}_{n,p} - D_{n,p}B_{n,p}) + i\hbar\Gamma_2 \sum_{n,p} (-1)^n \sqrt{\lambda_{n,p}}\,(A^{\dagger}_{n,p}B_{n,p} - A_{n,p}B^{\dagger}_{n,p})\,, \qquad (62)$$

where the operators $D_{n,p}$ characterize the difference optical frequency modes, called the Stokes component, the operators $A_{n,p}$ correspond to the anti-Stokes component of the sum frequency, and $B_{n,p}$ describe the THz radiation modes. We note that, in the term characterizing the generation of the sum frequency, an extra phase factor $(-1)^n$ arises, reflecting the fact that the produced anti-Stokes optical photon has the same azimuthal angle as the THz photon participating in the conversion.

Within an approach similar to that described in Section 2.2, the evolution of all photon creation operators in the Schmidt modes involved in Hamiltonian (62) is found and expressions for the mean number of photons in each beam are obtained. It turns out that, even in the case of the vacuum state for all modes at the entrance to the crystal, the mean number of anti-Stokes component photons at the exit from the crystal is not equal to zero but depends on the ratio of quadratic nonlinearities for the frequency down- and up-conversion processes. Importantly, in the high parametric gain regime, both processes occur not sequentially but simultaneously, thereby significantly increasing the efficiency of the sum frequency generation.

In [131], an integral of motion reflecting the noted mutual influence of processes was also obtained in the form of a combination of the photon number operators for the anti-Stokes ($\widehat{N}_{AS}$), THz ($\widehat{N}_i$), and Stokes ($\widehat{N}_S$) beams that is preserved during evolution:

$$\widehat{N}_{AS} + \widehat{N}_i - \widehat{N}_S = \widehat{N}^{in}_{AS} + \widehat{N}^{in}_i - \widehat{N}^{in}_S\,. \qquad (63)$$

Integral of motion (63) implies an important relation for the dispersion of the numbers of photons of the Stokes, anti-Stokes, and THz beams, which is valid in the case of initial vacuum states of all generated modes:

$$D_{N_{AS}-N_S} = D_{N_i}\,. \qquad (64)$$

This result means the occurrence of correlations in the number of photons between Stokes and anti-Stokes beams and allows studying the statistics of THz radiation photons based on measurements of only optical Stokes and anti-Stokes signals. It is also possible to obtain information about the correlations of THz and Stokes photons by analyzing the statistics of anti-Stokes ones. Such methods are important, because direct detection of THz signals is difficult.

The Stokes and anti-Stokes components can be correlated not only in the number of photons but also in azimuthal angles. In the case of one dominant radial mode, the covariance of Stokes and anti-Stokes photons in azimuthal angles can be found as [131]

$$\mathrm{cov}\,(\mathrm{S}, \mathrm{AS}) \sim \left| \sum_n \lambda_n G^2(\lambda_n G^2+1)\,\exp\left[in\left(\phi_s-(\pi+\phi_a)\right)\right] \right|^2. \qquad (65)$$

It follows from (65) that a strong azimuthal entanglement is established between Stokes and anti-Stokes photons that are emitted predominantly with opposite transverse components of the wave vectors. Figure 17 shows the distribution of covariance (65) with respect to the azimuthal angles of Stokes and anti-Stokes photons and the maximum of their correlation attained at $\phi_s - \phi_a = \pi$.

Thus, the mutual influence of frequency up- and down-conversion processes results in correlations in optical Stokes and anti-Stokes beams both in the number and in the azimuthal angle of photons. The correlations, which can be measured easily, allow extracting information about the properties of nonclassical light in the THz mode.

5. Anisotropy effects

The influence of the anisotropy of a nonlinear medium on parametric generation leads to so-called spatial drift. The effect of spatial (transverse) drift occurs because, in the general case, for extraordinarily polarized pumping, the Poynting vector corresponding to energy propagation and the wave vector have different directions inside the crystal due to birefringence. The effect of spatial drift, which turns out to be significant in the case of narrow pumping and long crystals, is usually parasitic. To eliminate it, a compensation setup is used that includes two nonlinear crystals with optical axes located in the same plane but at symmetric angles to the pump propagation direction, so as to eliminate the effect of spatial drift at the double crystal length. A similar setup without compensation but with the same length of the nonlinear medium just consists of two consecutive crystals with optical axes parallel to each other (Fig. 18a, b). The biphoton amplitude then has a different form for compensated and uncompensated anisotropy [79, 80]. Moreover, the anisotropy effects manifest themselves differently in low and high parametric gain.

In [81], the anisotropy effects were analyzed in the Schmidt mode formalism and, based on the analysis of the profiles and weights of the Schmidt modes, the output angular distributions of a squeezed vacuum in the collinear degenerate parametric scattering regime were obtained (see Fig. 18). As can be seen from Fig. 18c, at a low parametric gain and the same orientation of the optical axes in the crystals, the spatial drift effect leads to a strong asymmetry in the angular distribution of the generated squeezed light: the radiation is predominantly amplified in the drift direction. In this case, at angles symmetric with respect to the drift direction, an interference structure arises due to the induced coherence effect [80, 81, 140]. This effect can be explained as follows. Amplification of the signal beam occurs in the same direction at each point, along the direction of the Umov–Poynting vector of the pump. Due to the photon number correlation of twin beams, the idler radiation is also amplified, but in a symmetric direction, in accordance with the phase matching condition. However, it is generated in different, albeit collinear, directions at each point as the radiation propagates through the crystal. Thus, the total field in the idler channel has an interference structure. At the same time, anisotropy compensation allows obtaining an angular distribution of squeezed light that is symmetric with respect to the direction of collinear emission of photons (Fig. 18d).

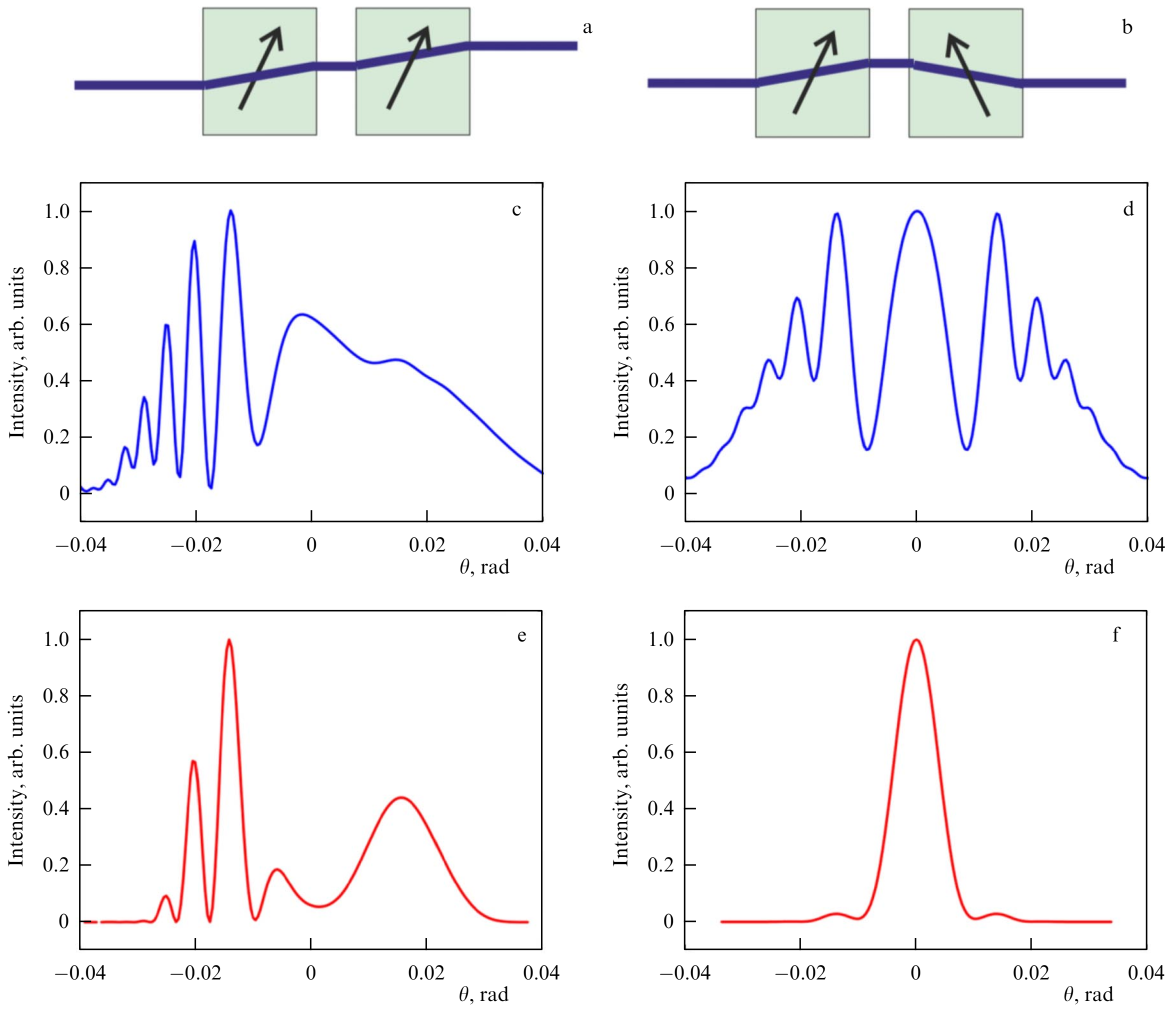

Figure 18. Crystal configurations (a) without and (b) with anisotropy compensation. (c, e) and (d, f) Angular distributions of the parametric scattering intensity in the collinear degenerate mode for the respective configurations, calculated for two values of the parametric gain: (c, d) $G = 10^{-4}$, (e, f) $G = 10$ [81]. Crystal length $L = 3$ mm, pump parameters $\lambda_p = 355$ nm and FWHM = 170 μm.

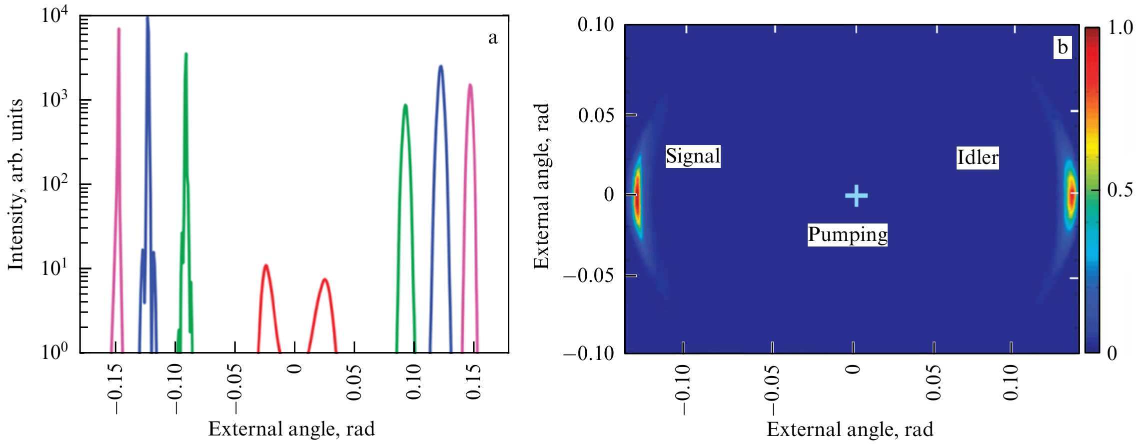

Figure 19. (a) Theoretical one-dimensional angular intensity profiles of parametric radiation for a fixed wavelength of 710 nm at various angles between the pump wave vector and the optical axis of a crystal: 33° (red), 34° (green), 34.9° (blue), and 36° (purple). (b) Measured intensity distribution corresponding to the formation of symmetric high-intensity peaks in the case of giant amplification; $L = 5$ mm, $\lambda_p = 350$ nm [141].

The picture changes at high values of the parametric gain coefficient: for uncompensated anisotropy in the regime of collinear degenerate phase matching, two narrower peaks appear due to the phase matching condition, one peak along the direction of the Umov–Poynting vector of the pump and the other in the direction symmetric to it (Fig. 18e). Moreover, when the crystal orientation changes, the condition for radiation amplification in the two conjugate directions is satisfied for different frequencies of the signal and idler beams. Thus, as a result of the anisotropy effect, it becomes possible to generate a two-color squeezed vacuum — high-intensity correlated twin beams at conjugate frequencies [81, 141].

Based on the anisotropy effect, a substantial change in the angular distribution of the generated squeezed vacuum and the buildup of two bright symmetric peaks detected at a fixed wavelength of parametric radiation with a change in the crystal orientation relative to the optical axis were observed experimentally and explained theoretically in [141].

The theoretically calculated one-dimensional angular profiles of the parametric radiation intensity obtained at a fixed wavelength of 710 nm for various crystal orientations (Fig. 19a) coincided with the measured ones with high accuracy [141]. As the crystal is detuned from the collinear phase-matching regime, the central peak splits into two peaks, whose intensity increases severalfold as the crystal rotation angle increases. At the angle of 34.9°, the phase-matching condition for the degenerate wavelength is satisfied at the drift angle, and therefore the peak intensity reaches its maximum at that orientation of the crystal, increasing by two to three orders of magnitude compared with the collinear phase-matching regime. The experimentally obtained intensity distribution corresponding to the degeneration of the ring structure into two symmetric high-intensity peaks in the case of giant amplification is shown in Fig. 19b. With a further increase in the rotation angle of the crystal relative to the optical axis, the intensity of the peaks starts decreasing. Thus, maximum-intensity radiation is generated in the crystal when the phase matching condition is satisfied for a given wavelength at the drift angle. In this case, turning the crystal allows selecting the wavelength at which the squeezed light is maximally amplified. From the standpoint of the Schmidt modes, the described situation is associated with a change in the mode weights and profiles: the distribution of the Schmidt weights for the drift angle is sharper, and the mode profiles are significantly narrowed, which leads to a sharp increase in the signal intensity for this crystal orientation in the high parametric gain regime. As a consequence, due to anisotropy effects, a giant amplification of the parametric scattering signal by several orders of magnitude occurs, which is observed at a certain frequency in the 'drift' direction.

6. Controlling the spectral properties of a bright squeezed vacuum

The spectral properties of squeezed light obtained in the process of parametric scattering are similar in a number of aspects to the features inherent in the spatial case. We first note the frequency correlations of signal and idler photons. Depending on the type of phase matching, a frequency-degenerate or nondegenerate parametric scattering regime is realized, with correlations between photons of the same or conjugate frequencies (which add up to the pump frequency).

The properties of the spectral distribution of biphotons obtained in the spontaneous parametric scattering regime were studied in [142–144]. The results of an experiment to determine the spectrum of the bright squeezed vacuum and measure correlations in the number of photons are described in [145], where the auto- and cross-covariance of the intensities were measured, depending on the wavelength of the signal and idler photons, and strong correlations of twin beams were also observed in the number of photons for conjugate wavelengths with the NRF of the difference signal, NRF $\ll 1$, much less than unity.

The theoretical analysis of the spectral characteristics of a squeezed vacuum is typically based either on the perturbation theory or on the introduction of broadband modes similar to Schmidt modes [71–73, 94].

The approach described in Section 2.3, also based on finding broadband frequency Schmidt modes and introducing the corresponding photon creation/annihilation operators, was used in [86, 110] to analyze the spectral properties of a squeezed vacuum. The found evolution of these operators in the Heisenberg representation allows calculating all the necessary characteristics of squeezed light if the Schmidt mode profiles are known. To control the spectral properties of the multiphoton squeezed vacuum just as in the spatial case, it is most promising to use a scheme with a nonlinear interferometer.

In [86, 110], the generation of a bright squeezed vacuum was analyzed in a scheme with a nonlinear Mach–Zehnder interferometer made of two successive nonlinear crystals separated by a medium with strong group velocity dispersion: SF_6 glass was used as the dispersing medium. In such a configuration, the radiation obtained in the process of parametric scattering in the first crystal can be amplified or attenuated in the second, depending on the phase relations between the pump and the signal and idler fields. When propagating through a medium with strong dispersion, the parametric scattering pulse generated in the first crystal spreads in time and becomes chirped due to the differences among the propagation speeds of different spectral components of the squeezed vacuum in a medium with group velocity dispersion [86, 110]. As a result of the chirping of the time pulse of the squeezed vacuum and the delay of the pump pulse in a dispersive medium, a nonlinear signal in only a certain spectral interval appears in the second crystal simultaneously with the pumping, and therefore amplification in the second crystal becomes possible for squeezed light of only a certain frequency range [86, 110]. Therefore, by changing the delay time of the pump pulse, it is possible to selectively amplify or attenuate certain spectral components and thereby vary the spectral composition of squeezed light.

As was established in the analysis of the relative phase shift acquired by the pumping and the signal and idler beams in the first crystal and in the dispersive medium, the condition for the frequency derivative of this phase to vanish determines the spectral interval in which the nonlinear signal overlapping with the pump pulse in the second crystal can be amplified, and the phase value itself is responsible for the condition of constructive or destructive interference. Thus, if the amplification condition is realized at a degenerate frequency, one central peak is observed in the spectrum, which is rather wide and rugged in the case of low parametric gain. If the amplification condition is satisfied for a nondegenerate spectral component, then two peaks appear in the spectrum, with the second one centered at the conjugate frequency; according to theoretical analysis, it should exhibit strong interference irregularity. The appearance of the second peak at the conjugate frequency is a direct consequence of photon correlations in conjugate twin beams, and sharp oscillations, similar in many respects to those described in Section 5, are due to the induced coherence effect.

All the above effects follow directly from the analysis carried out in terms of Schmidt modes and photon operators in these modes. Importantly, the mode profiles and their weight distributions depend significantly on the phase shift between the pump and the signal and idler beams. Moreover, for both the signal and idler channels, the dominant zero mode changes its structure from a single-peak one in the case of amplification at a degenerate frequency to an asymmetric two-peak one in the nondegenerate regime. In the degenerate regime, as the parametric gain coefficient increases, the distribution of mode weights narrows greatly, and the zero mode begins to dominate, such that only its contribution becomes significant and only one frequency mode is actually singled out in the high-gain limit. Moreover, in the high-gain regime, the profile width of this mode becomes very small. The frequency spectrum of the generated squeezed vacuum therefore becomes a very narrow peak, enhanced by several orders of magnitude compared to the spectrum in the spontaneous low-gain regime.

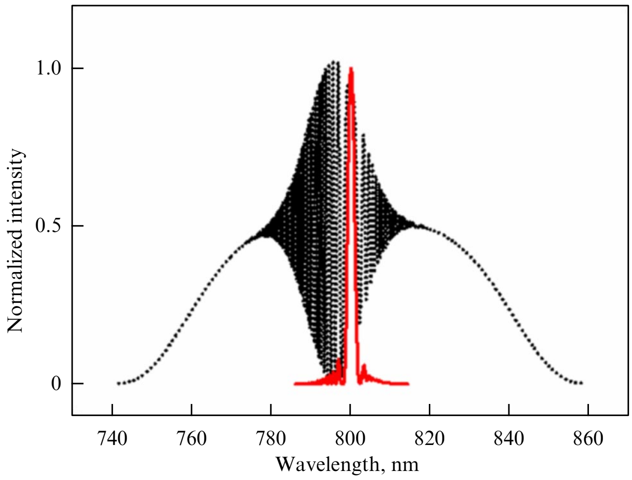

Figure 20. Spectral intensity of a squeezed vacuum calculated in the formalism of Schmidt modes in the case of amplification of degenerate spectral components in a nonlinear interferometer with parametric conversion coefficient $G = 1$ (black dots) and $G = 13$ (red solid curve) [86]. Crystal length $L = 3$ mm. The medium: $d = 36$ cm, SF_6 glass; $\lambda_s = 800$ nm, $\lambda_p = 400$ nm.

In Fig. 20, we show the normalized spectral intensity of the squeezed vacuum calculated in the Schmidt mode formalism in the case of amplification of degenerate spectral components in a nonlinear interferometer for low and high parametric gain [86]. It can be seen that a very narrow spectrum is formed at high gain, with amplification by several orders of magnitude (which is not shown in the figure due to the normalization of the function to unit height). As follows from an analysis of the second-order correlation function $g^{(2)}$, its value at $G = 13$ is close to 3, which implies the selection of one frequency mode and the generation of a single-mode squeezed vacuum [86].

We note that the described effects, obtained theoretically in the framework of the Schmidt mode formalism, were directly detected experimentally at low [146] and high [110] parametric gain. When the phase-matching condition corresponds to a nondegenerate frequency, at large values of the parametric conversion coefficient, two peaks remain in the spectrum of the bright squeezed vacuum, centered at conjugate frequencies; the peaks are narrow and are enhanced by several orders of magnitude (Fig. 21). The squeezed vacuum is actually enhanced only in two narrow spectral intervals selected by the phase-matching condition and controlled by the time delay of the pump pulse.

As can be seen from Fig. 21, an increase in the optical path of the pump leads to an increasingly greater detuning from the degenerate frequency, which allows the controlled selection of the frequencies of the squeezed-light twin beams. In addition to the experimental data, the figure shows the results of a calculation performed in the Schmidt mode formalism (red dashed-dotted curve), which are consistent with the experimental data. The inset shows an enlarged calculated interference structure of the right peak conjugate to the left peak for which the phase-matching condition is satisfied. Thus, the scheme with a nonlinear interferometer allows spectrum control and controlled selective generation of a two-color squeezed vacuum in a narrow spectral range with high gain.

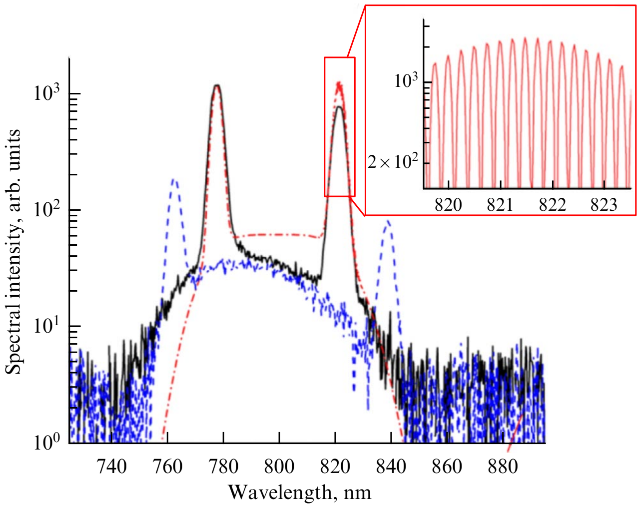

Figure 21. Spectral intensity of the squeezed vacuum generated in a nonlinear Mach–Zehnder interferometer with the optical pumping path increased compared to that in a frequency-degenerate configuration by 1.2 mm (black solid curve) and 2.4 mm (blue dashed curve), and the results of calculations in the Schmidt mode formalism in the case of the optical pumping path increased by 1.2 mm (red dashed-dotted curve) at parametric conversion coefficient $G = 7$ [110]. Inset shows the theoretically calculated interference structure of the conjugate peak. Crystal length $L = 3$ mm, pump parameters $\lambda_p = 400$ nm and FWHM = 600 µm, pulse duration $t = 0.9$ ps.

Theoretical analyses also showed that, in the case of a two-color squeezed vacuum in the high-gain limit, the contribution to the spectrum is made not by one Schmidt mode (as in the case of frequency-degenerate generation) but by two (symmetric and antisymmetric) modes having the same weights and spectral distributions but differing in parity with respect to the position of the degenerate frequency. In the case under consideration, the calculated theoretical value of the second-order correlation function is $g^{(2)} = 3/2$ [86]. This effect is analogous to the doubling of the weight coefficients of the spatial radial Schmidt modes (see Fig. 9) discussed in Section 3.2.

The above-described control of the spectral properties of a squeezed vacuum is related, in one way or another, to a decrease in the effective number of Schmidt modes and the dominant contribution of one or several lower modes. A separate interesting, but rather difficult problem is to develop methods to vary the weights of the Schmidt modes by changing the dominant character of a particular mode. Importantly, this must not introduce losses that destroy photon correlations. A possible solution to this problem is based on a scheme in which squeezed light is used as a seed of the signal mode and is transformed in the process of the sum-frequency generation (SFG) [147, 148]. Using such a scheme, called a quantum pulse gate, it is possible to selectively block any Schmidt mode of the squeezed vacuum by completely converting it into the frequency sum mode [149–152]. This scheme is also promising as regards solving problems in quantum tomography [153, 154].

We consider the principle of operation of a quantum optical gate using the example of a degenerate SFG regime, when the pump and the input signal photon frequencies coincide, and their sum corresponds to the frequency of the generated 'output' photon. To analyze this nonlinear process, we can also use the formalism of Schmidt modes and describe the signal and output fields using Schmidt modes. Due to the short duration of the pump pulse, a single-mode regime is realized for each field [149, 150], and in that case the SFG Hamiltonian can be written as

$$\widehat{H}_{\mathrm{SFG}} = \mathrm{i}\hbar\Gamma_1(\widehat{D}\widehat{C}^{\dagger} - \widehat{D}^{\dagger}\widehat{C})\,, \tag{66}$$

where $C^{\dagger}$ and $\widehat{D}$ are the photon creation and annihilation operators in the respective sum-frequency mode and signal mode. The spectral profile of the output high-frequency mode is determined by the crystal parameters and tuning, while the converted signal mode corresponds to the pump frequency spectrum. Mathematically, Hamiltonian (66) corresponds to a beam-splitter Hamiltonian, and the input and output operators in the Heisenberg representation are related by a standard transformation in terms of the beam-splitter matrix, with the transmission and reflection probabilities respectively expressed as $\cos^2\Theta$ and $\sin^2\Theta$,

$$\begin{pmatrix}\widehat{C}^{\mathrm{out}}\\ \widehat{D}^{\mathrm{out}}\end{pmatrix} = \begin{pmatrix}\cos\Theta & \sin\Theta\\ -\sin\Theta & \cos\Theta\end{pmatrix}\begin{pmatrix}\widehat{C}^{\mathrm{in}}\\ \widehat{D}^{\mathrm{in}}\end{pmatrix}, \tag{67}$$

where $\Theta = \int\Gamma_1\,\mathrm{d}t$ is the so-called beam-splitter angle characterizing its transmission and reflection. We can see that the field in the signal mode is not completely converted into a high-frequency signal in the general case. The complete transformation occurs at the angle $\pi/2$. It is not difficult to obtain expressions for the mean numbers of output photons in the modes. When the vacuum is at the input for the sum-frequency mode, the mean numbers of photons in the high-frequency and signal modes, $\langle\widehat{N}_{\mathrm{SF}}^{\mathrm{out}}\rangle$ and $\langle\widehat{N}_{\mathrm{s}}^{\mathrm{out}}\rangle$, follow from the transformation of only the input number of photons in the signal mode $\langle\widehat{N}_{\mathrm{s}}^{\mathrm{in}}\rangle$ [150],

$$\langle\widehat{N}_{\mathrm{SF}}^{\mathrm{out}}\rangle = \sin^2\Theta\langle\widehat{N}_{\mathrm{s}}^{\mathrm{in}}\rangle\,, \tag{68}$$

$$\langle\widehat{N}_{\mathrm{s}}^{\mathrm{out}}\rangle = \cos^2\Theta\langle\widehat{N}_{\mathrm{s}}^{\mathrm{in}}\rangle\,. \tag{69}$$

Let the multimode squeezed vacuum generated in the frequency-degenerate regime of parametric scattering and characterized by a set of frequency modes be fed to the entrance to the signal channel of a quantum-optical gate. If one of the Schmidt frequency modes of the squeezed vacuum coincides with the Schmidt mode of the signal channel, then, under the condition $\Theta = \pi/2$, photons in the squeezed vacuum mode are completely converted into the sum-frequency signal, while the other modes not involved in this process pass without change. Thus, it is possible to block a certain Schmidt mode of a squeezed vacuum by the quantum-optical method with minimal losses. Because the frequency profile of the signal mode of a quantum-optical gate coincides with the spectral profile of classical pumping, varying the pumping spectrum allows selectively 'tuning' to one blocked Schmidt mode or another of the squeezed vacuum. Selective blocking of frequency Schmidt modes was described theoretically and demonstrated experimentally in [149, 150].

Further development of this approach and its generalization to the case where several Schmidt modes of a squeezed vacuum are involved in the transformation in a mode gate is described in [155]. Depending on the transformation angle Θ and the overlap of the spectral profiles of the converted Schmidt modes and the gate signal mode, one can obtain a different number of photons in these modes at the output of the quantum optical gate and thus change their relative

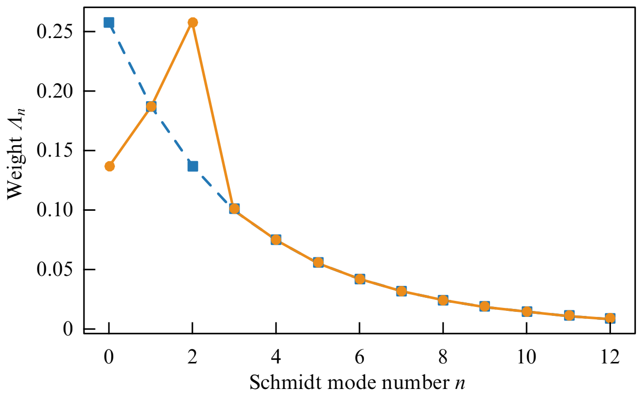

Figure 22. Weight distribution of squeezed vacuum Schmidt modes: initial (blue squares: monotonic dependence, parametric gain 6.5) and after the transformation of the zero and second Schmidt modes in a quantum optical gate at angle $\Theta = \pi$ (yellow dots: nonmonotonic dependence) [155].

contributions (weights). In the framework of the developed approach, the possibilities of exchanging weights between a pair of modes, of selectively increasing the contribution of a certain mode, etc., have been demonstrated.

Figure 22 shows the redistribution of the Schmidt mode weights for a squeezed vacuum after the transformation of the zeroth and second Schmidt modes in a quantum optical gate at the angle $\Theta = \pi$, when no high-frequency mode is generated [155]. It can be seen from the figure that, as a result of such a transformation, the zeroth and second modes exchange weights and the second mode becomes dominant, while the initial mode weights monotonically decrease with increasing mode number. Thus, this scheme allows controlling the weights of the Schmidt frequency modes of the bright squeezed vacuum over a wide range.

To conclude this section, we note that considering the spatial or spectral properties of the bright squeezed vacuum separately is not always correct because of the entanglement and mutual influence of these degrees of freedom. Most of the effects discussed in this review, described in terms of either frequency or spatial settings, are in very good agreement with experimental data. However, broadening of the spatial or spectral distribution of a squeezed vacuum generated in a single crystal with increasing parametric gain [145], predicted theoretically in [1] and observed experimentally, was not obtained in the framework of the approach in Section 2. For a theoretical analysis of this effect, an approach has been developed where spatial and spectral degrees of freedom are considered simultaneously and their mutual influence is taken into account [107]. This approach involves solving integro-differential equations for photon operators, depending on spatial and temporal variables. In the case of generation in a single nonlinear crystal, a broadening of the angular distribution of the bright squeezed vacuum with an increase in the parametric gain was found, which led to an increase in the FWHM by almost a factor of 1.5 in the high-gain limit. From the standpoint of the Schmidt modes, this fact means that their dependence on the parametric gain is not too strong, but still noticeable.

We note that, in the scheme with a nonlinear interferometer, such broadening does not occur; instead, the highest peaks in the spatial or spectral distribution are amplified and dominate, indicating, on the contrary, a narrowing of the angular or frequency spectrum and the tendency to select one Schmidt mode [107]. Thus, we can conclude that the approach considered in Section 2 is indeed valid for a nonlinear interferometer: the Schmidt modes are independent of the gain coefficient, and only their weights change as it increases.

In [156–158], an attempt was also made to unify the analysis of the spatial and spectral properties of the squeezed vacuum. However, many of the results obtained were explained as a consequence of the pump depletion effect, and in some cases the analysis was carried out in terms of the dynamics of the mean values of the photon and field operators [157, 158].

The results of an experimental study of quadrature squeezing in various space–time modes of a squeezed vacuum in [103] have already been discussed in Section 2.5. We note that, in the experiment, the spatial properties were studied for each spectral mode separately and hence a specific spatial mode was selected for the analysis of spectral properties. Thus, the results obtained do not allow drawing detailed conclusions about the mutual influence of the spatial and spectral degrees of freedom of squeezed light.

A theoretical study of squeezing in space–time modes of a squeezed vacuum was carried out in [159] both numerically and analytically using Gaussian functions in curvilinear coordinates to approximate the biphoton amplitude. The results obtained confirmed the conclusion in [107] about the impossibility of factorization of space–time degrees of freedom in the general case and about the strong entanglement between them, which is especially important in the limit of an ultrashort pump pulse duration.

7. High-precision measurements using squeezed light

The use of biphoton pairs and multiphoton squeezed states opens up new possibilities for a number of applied problems in the field of quantum communication, quantum information technologies, metrology, and others, discussing which would require writing a separate review. We briefly consider the prospects for using squeezed fields in linear and nonlinear interferometers. The use of squeezed light in optical interferometers for measurements with an accuracy exceeding the standard quantum limit, as well as in gravitational wave detectors, is discussed in detail in [160].

The correlations among photons allows carrying out high-precision measurements with a very low noise level. Indeed, due to the presence of strong correlations, the change in the number of photons in conjugate beams occurs synchronously, and hence the dispersion of their difference is minimized, to become much less than shot noise. If a weak disturbance which is to be measured arises in one of the correlated channels inside the interferometer, then the calculation of the difference between the numbers of photons in the signal and idler beams (according to the coincidence scheme) gives the desired signal with a high degree of accuracy due to subtraction of the noises, which are the same in the conjugate beams.

As discussed in the foregoing, the setup with a nonlinear interferometer allows controlling the profiles and weights of the Schmidt modes both in space and in frequency, and hence allows controlling the spatial and spectral/temporal correlations of photons. With the interferometer setup, the unknown properties of a medium placed inside the interferometer can be measured with high accuracy (due to interference), similarly to the case of finding the dispersion characteristics of the intermediate layer in the THz range, as described in Section 4.2 for strongly frequency-nondegenerate parametric scattering. It is important that photon correlations in the signal and idler channels allow obtaining all information in the THz range from measurements in the optical channel.

The scheme with a nonlinear interferometer has a high sensitivity to the relative phase between the pump and the signal and idler fields. Therefore, even a weak phase perturbation can be measured with high accuracy due to correlations in the number of photons in conjugate beams and quadrature squeezing [59, 61, 161, 162], because the output signal depends nonlinearly on the phase and can be significantly amplified, while the noise due to quadrature squeezing is below the shot noise level [59, 61, 161, 162].

For the interferometer scheme, the accuracy of measuring the phase $\Delta\phi$, which depends significantly on the photon statistics of the light used, satisfies the uncertainty relation

$$\Delta N \Delta\phi \geqslant 1\,, \tag{70}$$

where ΔN is the uncertainty in the number of photons in a given state of the electromagnetic field. In the case of coherent fields with the mean number of photons N, the limit measurement accuracy corresponds to the shot noise level [163]:

$$\Delta\phi_{\mathrm{SNL}} = \frac{1}{\sqrt{N}}\,. \tag{71}$$

Superresolution can be achieved when using coherently squeezed light with not too much squeezing, which allows overcoming the shot noise level [60]:

$$\Delta\phi \gtrsim \frac{\exp(-R)}{\sqrt{N}}\,. \tag{72}$$

In highly squeezed fields close to a squeezed vacuum, the relation

$$\exp(-R) \sim \frac{1}{\sqrt{N}} \tag{73}$$

allows the Heisenberg limit to be approached:

$$\Delta\phi \gtrsim \frac{1}{N}\,. \tag{74}$$

Various configurations of interference schemes using squeezed light were analyzed in detail in [60]; the ones with external illumination, as well as those implementing squeezing of conjugate field quadratures at the entrance to and exit from the interferometer (i.e., squeezing of a certain quadrature in the first crystal and so-called anti-squeezing in the second), were found to be optimal.

A scheme of an 'unbalanced' nonlinear interferometer was also proposed, in which the gain in the second crystal is almost twice that in the first crystal. It has been demonstrated that such a scheme is not very sensitive to external losses, and the high accuracy of phase measurements is preserved even at up to 80% detection losses [59].

In [164, 165], a nonlinear interferometer was used for high-precision detection of angular rotations and perturbations of the angular coordinate, realized due to the twisting of squeezed light and the correlation of photons in modes with opposite OAM projection values. Phase measurements with a noise level much less than shot noise have also been demonstrated for a wide-angle multimode SU(1,1) interferometer with an effective number of modes greater than 100 [106]. The implementation of optimal regimes in terms of high phase sensitivity and visibility in a multimode SU(1,1) interferometer was analyzed in [166].

8. Conclusion

We have discussed the spatial and spectral features of nonclassical electromagnetic fields in a squeezed vacuum state, as well as photon correlations in such fields. Correlations of photons and a number of unique properties of squeezed states make them indispensable for practical applications in quantum information technologies, coding and transmission of quantum information, optomechanics, quantum metrology, quantum imaging, and high-precision measurements with an extremely low noise level. At the same time, squeezed fields are very fragile objects, extremely sensitive to losses, which requires precision experiments and the development of special quantum-optical methods for controlling their properties. The bright squeezed vacuum is actually a macroscopic quantum state with a large number of photons in each mode, which greatly complicates its theoretical analysis. Today, the most promising theoretical approach is apparently that based on the introduction of independent Schmidt modes and photon operators in them. It allows correctly describing such states and gives good agreement with experimental data.

Possible applications of squeezed states are not limited to the above problems. Another important and already developing area is the interaction of such states with various media, atoms, molecules, and nanostructured objects. An increase in the probability of multiphoton processes under the action of a squeezed vacuum field has already been registered in experiments on the generation of two to four harmonics [167]. The discovery of many more new physical effects associated with the nonclassical properties of such fields can also be expected.

The authors express their deep gratitude to Maria Vladimirovna Chekhova for the fruitful joint research and useful discussions, without which this review could hardly have been written.

The study was financially supported by the Russian Foundation for Basic Research (project no. 20-12-50326), the Basis Foundation (grant no. 21-1-5-32-1), and the Development Program of the Interdisciplinary Research and Education School, Photon and quantum technologies. Digital medicine, Lomonosov Moscow State University.

References

1. Klyshko D N *Photons and Nonlinear Optics* (New York: Gordon and Breach, 1988); Translated from Russian: Klyshko D N *Fotony i Nelineinaya Optika* (Moscow: Nauka, 1980)
2. Belinsky A V, Klyshko D N *Laser Phys.* **4** 663 (1994)
3. Klyshko D N *Sov. Phys. JETP* **56** 753 (1982); *Zh. Eksp. Teor. Fiz.* **83** 1313 (1982)
4. Klyshko D N *JETP Lett.* **6** 23 (1967); *Pis'ma Zh. Eksp. Teor. Fiz.* **6** 490 (1967)
5. Akhmanov S A et al. *JETP Lett.* **6** 85 (1967); *Pis'ma Zh. Eksp. Teor. Fiz.* **6** 575 (1967)
6. Harris S E, Oshman M K, Byer R L *Phys. Rev. Lett.* **18** 732 (1967)
7. Magde D, Mahr H *Phys. Rev. Lett.* **18** 905 (1967)
8. Zel'dovich B Ya, Klyshko D N *JETP Lett.* **9** 40 (1969); *Pis'ma Zh. Eksp. Teor. Fiz.* **9** 69 (1969)

9. Burnham D C, Weinberg D L *Phys. Rev. Lett.* **25** 84 (1970)
10. Krivitskii L A et al. *J. Exp. Theor. Phys.* **97** 846 (2003); *Zh. Eksp. Teor. Fiz.* **124** 943 (2003)
11. Molina-Terriza G, Torres J P, Torner L *Phys. Rev. Lett.* **88** 013601 (2002)
12. Vaziri A et al. *Phys. Rev. Lett.* **88** 227902 (2003)
13. Langford N K et al. *Phys. Rev. Lett.* **93** 053601 (2004)
14. Bogdanov Yu I et al. *Phys. Rev. Lett.* **93** 230503 (2004)
15. Neves L et al. *Phys. Rev. Lett.* **94** 100501 (2005)
16. O'Sullivan-Hale M N et al. *Phys. Rev. Lett.* **94** 220501 (2005)
17. Fedorov M V et al. *Phys. Rev. Lett.* **99** 063901 (2007)
18. D'Ariano G M, Mataloni P, Sacchi M F *Phys. Rev. A* **71** 062337 (2005)
19. Moreva E et al. *Phys. Rev. Lett.* **97** 023602 (2006)
20. Bogdanov Yu I et al. *Phys. Rev. A* **73** 063810 (2006)
21. Baek S-Y et al. *Phys. Rev. A* **78** 042321 (2008)
22. Fedorov M V et al. *Phys. Rev. A* **77** 032336 (2008)
23. Fedorov M V et al. *New J. Phys.* **13** 083004 (2011)
24. Fedorov M V, Volkov P A, Mikhailova J M *J. Exp. Theor. Phys.* **115** 15 (2012); *Zh. Eksp. Teor. Fiz.* **142** 20 (2012)
25. Saygin M Yu, Chirkin A S, Kolobov M I *J. Opt. Soc. Am. B* **29** 2090 (2012)
26. Wooters W K *Phys. Rev. Lett.* **80** 2245 (1998)
27. Vidal G, Werner R F *Phys. Rev. A* **65** 032314 (2002)
28. Bouwmeester D et al. *Nature* **390** 575 (1997)
29. Kim Y-H, Kulik S P, Shih Y *Phys. Rev. Lett.* **86** 1370 (2001)
30. Brida G et al. *Phys. Rev. A* **76** 053807 (2007)
31. Shurupov A P et al. *Europhys. Lett.* **87** 10008 (2009)
32. Jack B et al. *New J. Phys.* **11** 103024 (2009)
33. Bogdanov Yu I et al. *Phys. Rev. Lett.* **105** 010404 (2010)
34. Bogdanov Yu I, Kulik S P *Laser Phys. Lett.* **10** 125202 (2013)
35. Kravtsov K S et al. *Phys. Rev. A* **87** 062122 (2013)
36. Pan J-W et al. *Rev. Mod. Phys.* **84** 777 (2012)
37. Bondani M et al. *Phys. Rev. A* **76** 013833 (2007)
38. Iskhakov T Sh et al. *JETP Lett.* **88** 660 (2008); *Pis'ma Zh. Eksp. Teor. Fiz.* **88** 757 (2008)
39. Chuprina I N, Kalachev A A *Phys. Rev. A* **100** 043843 (2019)
40. Kalachev A et al. *Laser Phys.* **29** 104001 (2019)
41. Iskhakov T, Chekhova M V, Leuchs G *Phys. Rev. Lett.* **102** 183602 (2009)
42. Spasibko K Yu, Iskhakov T Sh, Chekhova M V *Opt. Express* **20** 7507 (2012)
43. Iskhakov T Sh et al. *Opt. Lett.* **37** 1919 (2012)
44. Chekhova M V, Leuchs G, Żukowski M *Opt. Commun.* **337** 27 (2015)
45. Eibl M et al. *Phys. Rev. Lett.* **90** 200403 (2003)
46. Rådmark M, Zukowski M, Bourennane M *Phys. Rev. Lett.* **103** 150501 (2009)
47. Stobińska M et al. *Phys. Rev. A* **86** 022323 (2012)
48. Karassiov V P *J. Phys. A* **26** 4345 (1993)
49. Karassiov V P, Masalov A V *Opt. Spectrosc.* **74** 551 (1993); *Opt. Spektrosk.* **74** 928 (1993)
50. Bushev P A et al. *Opt. Spectrosc.* **91** 526 (2001); *Opt. Spektrosk.* **91** 558 (2001)
51. Brida G et al. *Opt. Express* **18** 20572 (2010)
52. Brida G, Genovese M, Ruo Berchera I *Nat. Photon.* **4** 227 (2010)
53. Lopaeva E D et al. *Phys. Rev. Lett.* **110** 153603 (2013)
54. Kolobov M I *Quantum Imaging* (New York: Springer, 2007); Translated into Russian: Kolobov M I (Ed.) *Kvantovoe Izobrazhenie* (Translated into Russian by T Yu Golubeva, Ed. A S Chirkin) (Moscow: Fizmatlit, 2009)
55. Magnitskiy S, Agapov D, Chirkin A *Opt. Lett.* **47** 754 (2022)
56. Khalili F et al. *Phys. Rev. Lett.* **105** 070403 (2010)
57. Anderson B E et al. *Optica* **4** 752 (2017)
58. Gong Q-K et al. *Phys. Rev. A* **96** 033809 (2017)
59. Manceau M et al. *Phys. Rev. Lett.* **119** 223604 (2017)
60. Manceau M, Khalili F Ya, Chekhova M *New J. Phys.* **19** 013014 (2017)
61. Knyazev E et al. *New J. Phys.* **20** 013005 (2018)
62. Knyazev E, Khalili F Ya, Chekhova M V *Opt. Express* **27** 7868 (2019)
63. Shaked Y et al. *Nat. Commun.* **9** 609 (2018)
64. Mikhailova Yu M, Volkov P A, Fedorov M V *Phys. Rev. A* **78** 062327 (2008)
65. Fedorov M V, Mikhailova Yu M, Volkov P A *J. Phys. B* **42** 175503 (2009)
66. Chekhova M V, Fedorov M V *J. Phys. B* **46** 095502 (2013)
67. Fedorov M V, Miklin N I *Contemp. Phys.* **55** 94 (2014)
68. Fedorov M V *Phys. Rev. A* **93** 033830 (2016)
69. Fedorov M V et al. *Phys. Rev. A* **98** 013850 (2018)
70. Fedorov M V *Phys. Rev. A* **97** 012319 (2018)
71. Wasilewski W et al. *Phys. Rev. A* **73** 063819 (2006)
72. Christ A et al. *New J. Phys.* **15** 053038 (2013)
73. Eckstein A, Brecht B, Silberhorn Ch *Opt. Express* **19** 13770 (2011)
74. Brambilla E et al. *Phys. Rev. A* **69** 023802 (2004)
75. Brambilla E et al. *Phys. Rev. A* **77** 053807 (2008)
76. Brambilla E et al. *Phys. Rev. A* **82** 013835 (2010)
77. Rubin M H *Phys. Rev. A* **54** 5349 (1996)
78. Wang L J, Hong C K, Friberg S R *J. Opt. B* **3** 346 (2001)
79. Pérez A M et al. *Laser Phys. Lett.* **10** 125201 (2013)
80. Cavanna A et al. *Opt. Express* **22** 9983 (2014)
81. Sharapova P et al. *Phys. Rev. A* **91** 043816 (2015)
82. Miatto F M et al. *Eur. Phys. J. D* **66** 263 (2012)
83. Miatto F M, Brougham T, Yao A M *Eur. Phys. J. D* **66** 183 (2012)
84. Law C K, Eberly J H *Phys. Rev. Lett.* **92** 127903 (2004)
85. Rytikov G O, Chekhova M V *J. Exp. Theor. Phys.* **107** 923 (2008); *Zh. Eksp. Teor. Fiz.* **134** 1082 (2008)
86. Sharapova P R et al. *Phys. Rev. A* **97** 053827 (2018)
87. Schmidt E *Math. Ann.* **63** 433 (1907); Translated into English with commentary by G W Stewart: http://users.umiacs.umd.edu/˜stewart/FHS.pdf
88. Grobe R, Rzazewski K, Eberly J H *J. Phys. B* **27** L503 (1994)
89. Ekert A, Knight P *Am. J. Phys.* **63** 415 (1995)
90. Law C K, Walmsley I A, Eberly J H *Phys. Rev. Lett.* **84** 5304 (2000)
91. Fedorov M V et al. *Phys. Rev. A* **72** 032110 (2005)
92. Mercer J *Philos. Trans. R. Soc. Lond. A* **209** 415 (1909)
93. Beltran L et al. *J. Opt.* **19** 044005 (2017)
94. Dayan B *Phys. Rev. A* **76** 043813 (2007)
95. Agafonov I N, Chekhova M V, Leuchs G *Phys. Rev. A* **82** 011801 (2010)
96. Heidmann A et al. *Phys. Rev. Lett.* **59** 2555 (1987)
97. Brida G et al. *Phys. Rev. Lett.* **102** 213602 (2009)
98. Harder G et al. *Phys. Rev. Lett.* **116** 143601 (2016)
99. Agarwal G S *Quantum Optics* (Cambridge: Cambridge Univ. Press, 2013)
100. Lvovsky A I "Squeezed light," in *Photonics* Vol. 1 (Ed. D Andrews) (Hoboken, NJ: John Wiley and Sons, 2015) p. 121; arXiv:1401.4118
101. Zakharov R V, Tikhonova O V *Laser Phys. Lett.* **15** 055205 (2018)
102. Fedorov M V *Laser Phys.* **29** 124006 (2019)
103. La Volpe L et al. *Opt. Express* **28** 12385 (2020)
104. Treps N et al. *Phys. Rev. Lett.* **88** 203601 (2002)
105. Embrey C S et al. *Phys. Rev. X* **5** 031004 (2015)
106. Frascella G et al. *Optica* **6** 1233 (2019)
107. Sharapova P R et al. *Phys. Rev. Res.* **2** 013371 (2020)
108. Pérez A M et al. *Opt. Lett.* **39** 2403 (2014)
109. Hudelist F et al. *Nat. Commun.* **5** 3049 (2014)
110. Lemieux S et al. *Phys. Rev. Lett.* **117** 183601 (2016)
111. Klyshko D N *J. Exp. Theor. Phys.* **78** 848 (1994); *Zh. Eksp. Teor. Fiz.* **105** 1574 (1994)
112. Ivanova O A et al. *Quantum Electron.* **36** 951 (2006); *Kvantovaya Elektron.* **36** 951 (2006)
113. Frascella G et al. *Laser Phys.* **29** 124013 (2019)
114. Marino A M et al. *Phys. Rev. Lett.* **101** 093602 (2008)
115. Mair A et al. *Nature* **412** 313 (2001)
116. Berkhout G C G et al. *Phys. Rev. Lett.* **105** 153601 (2010)
117. Zakharov R V, Tikhonova O V *Bull. Russ. Acad. Sci. Phys.* **82** 1388 (2018); *Izv. Ross. Akad. Nauk Fiz.* **82** 1525 (2018)
118. Ma G H et al. *J. Opt. Soc. Am. B* **23** 81 (2006)
119. Kitaeva G Kh, Penin A N, Tuchak A N *Opt. Spectrosc.* **107** 521 (2009); *Opt. Spektrosk.* **107** 553 (2009)
120. Wang T D et al. *Opt. Express* **16** 6471 (2008)
121. Kornienko V V et al. *Opt. Lett.* **41** 4075 (2016)
122. Kitaeva G Kh et al. *Opt. Lett.* **44** 1198 (2019)
123. Klyshko D N *Sov. J. Quantum Electron.* **7** 591 (1977); *Kvantovaya Elektron.* **4** 1056 (1977)

124. Kitaeva G Kh et al. *Appl. Phys. B* **116** 929 (2014)
125. Kitaeva G Kh, Kornienko V V *Int. J. Quantum Inf.* **15** 1740024 (2017)
126. Kornienko V V et al. *APL Photon.* **3** 051704 (2018)
127. Kitaeva G Kh, Penin A N *J. Exp. Theor. Phys.* **98** 272 (2004); *Zh. Eksp. Teor. Fiz.* **125** 307 (2004)
128. Kitaeva G Kh et al. *J. Infrared Millimeter Terahertz Waves* **32** 1144 (2011)
129. Kitaeva G Kh *Phys. Rev. A* **76** 043841 (2007)
130. Kitaeva G Kh et al. *Phys. Rev. A* **98** 063844 (2018)
131. Zakharov R V, Tikhonova O V *Laser Phys.* **29** 124010 (2019)
132. Kuznetsov K A et al. *Phys. Rev. A* **101** 053843 (2020)
133. Abdullin U A et al. *Sov. Phys. JETP* **39** 633 (1974); *Zh. Eksp. Teor. Fiz.* **66** 1295 (1974)
134. Klyshko D N *J. Exp. Theor. Phys.* **77** 222 (1993); *Zh. Eksp. Teor. Fiz.* **104** 2676 (1993)
135. Korystov D Y, Kulik S P, Penin A N *Quantum Electron.* **30** 922 (2000); *Kvantovaya Elektron.* **30** 922 (2000)
136. Kalashnikov D A et al. *Nat. Photon.* **10** 98 (2016)
137. Rasputnyi A V, Kopylov D A *Phys. Rev. A* **104** 013702 (2021)
138. Aleksandrovski A L, Chirkin A S, Volkov V V *J. Russ. Laser Res.* **18** 101 (1997)
139. Dmitriev V G, Tarasov L V *Prikladnaya Nelineinaya Optika* 2nd ed., rev., enl. (Moscow: Fizmatlit, 2004)
140. Kolobov M I et al. *J. Opt.* **19** 054003 (2017)
141. Pérez A M et al. *Nat. Commun.* **6** 7707 (2015)
142. Kim Y-H, Grice W P *Opt. Lett.* **30** 908 (2005)
143. Poh H S et al. *Phys. Rev. A* **75** 043816 (2007)
144. Baek S-Y, Kim Y-H *Phys. Rev. A* **77** 043807 (2008)
145. Spasibko K Yu, Iskhakov T Sh, Chekhova M V *Opt. Express* **20** 7507 (2012)
146. Iskhakov T Sh et al. *J. Mod. Opt.* **63** 64 (2016)
147. Reddy D V, Raymer M G *Opt. Express* **25** 12952 (2017)
148. Shahverdi A et al. *Sci. Rep.* **7** 6495 (2017)
149. Brecht B et al. *New J. Phys.* **13** 065029 (2011)
150. Eckstein A, Brecht B, Silberhorn C *Opt. Express* **19** 13770 (2011)
151. Manurkar P et al. *Optica* **3** 1300 (2016)
152. Allgaier M et al. *Phys. Rev. A* **101** 043819 (2020)
153. Ansari V et al. *Phys. Rev. A* **96** 063817 (2017)
154. Ansari V et al. *Phys. Rev. Lett.* **120** 213601 (2018)
155. Sukharnikov V, Sharapova P, Tikhonova O *Opt. Laser Technol.* **136** 106769 (2021)
156. Peřina J (Jr.) *Phys. Rev. A* **92** 013833 (2015)
157. Peřina J (Jr.) *Phys. Rev. A* **93** 013852 (2016)
158. Peřina J (Jr.) et al. *Sci. Rep.* **6** 22320 (2016)
159. La Volpe L et al. *Phys. Rev. Appl.* **15** 024016 (2021)
160. Schnabel R *Phys. Rep.* **684** 1 (2017)
161. Ou Z Y *Phys. Rev. A* **85** 023815 (2012)
162. Anderson B E et al. *Optica* **4** 752 (2017)
163. Yurke B, McCall S L, Klauder J R *Phys. Rev. A* **33** 4033 (1986)
164. Jha A K et al. *Phys. Rev. A* **83** 053829 (2011)
165. Liu J et al. *J. Opt.* **20** 025201 (2018)
166. Frascella G et al. *Opt. Lett.* **46** 2364 (2021)
167. Spasibko K Yu et al. *Phys. Rev. Lett.* **119** 223603 (2017)